Chapter 5

Mid-IR observations of circumstellar dust

The previous chapters show how the analysis of the spectral energy distribution depends on the spatial distribution of the dust around the central source. Temporal variations in the mass loss rate give rise to complex radial density profiles, and thus affect the thermal structure and source spectra. Moreover, there are evidences of departures from spherical symmetry in many classes of circumstellar envelopes. Envelopes around Young Stellar Objects (YSOs) are formed in presence of dust disks or tori, and in many cases are perturbed by collimated molecular outflows. AGB stars are the precursors of Planetary Nebulæ, which show a wide array of axisymmetric, point symmetric or completely asymmetric shapes. It is not clear at which point of the transition between the AGB phase and PN the spherical symmetry is lost. Since a few AGB stars observed with high spatial resolution (Karovska et al., 1997; Lopez et al., 1997; Weigelt et al., 1998) do show asymmetric structures, it is not unlikely to imagine non spherical perturbations in the dusty envelopes during the AGB.

In this chapter the perspective of high resolution imaging of circumstellar envelopes with state of the art mid-IR imaging cameras are explored. The results obtained with several instruments at different telescopes are presented.

Section 5.3 describes the observations of a sample of AGB circumstellar envelopes performed with the mid-IR cameras TIRCAM (Tirgo InfraRed CAMera) and CAMIRAS at the TIRGO (Telescopio InfRarosso al GOrnergrat, Switzerland) and San Pedro Martir (SPM, Observatorio Astronomico National, Mexico) telescopes. These observations, are aimed to test the

discriminating capability between the chemical and physical status of AGB envelopes with mid-IR observations. They have been made in collaboration with the TIRCAM and CAMIRAS team from 1992 to 1997, have been presented at several International Workshops and Meetings, and published in the papers Busso et al. (1996), Marengo et al. (1997) and Marengo et al. (1999).

Section 5.4 shows a new set of observations made with the camera MIRAC3 at the NASA Infrared Telescope Facility (IRTF, Mauna Kea, Hawaii). This project, was done under the supervision of Giovanni G. Fazio at the Harvard-Smithsonian Center for Astrophysics, in collaboration with the MIRAC team (G.G Fazio, W.F. Hoffmann, J.L Hora, A. Dayal and L.K. Deutsch). The goal of the project was to obtain direct information on the spatial structure of dusty circumstellar envelopes around AGB stars. The results have been presented at the International Conference "Asymmetrical Planetary Nebulæ II: from Origins to Microstructures", Cambridge MA, August 3-6, 1999 (see Marengo et al., 2000b). A paper is in preparation, discussing the detection of extended envelope emissions for a number of sources, and the constraints that the images provide for the geometry of the observed circumstellar envelopes.

In section 5.5, the observation of circumstellar dust around the massive YSO AFGL 2591 is described. The images, taken with MIRAC3 at IRTF in collaboration with the MIRAC team and Ray Jayawardhana, show the detection of a dust knot which may be evidence of a recent ejection event, in a source characterized by a well known molecular outflow. The results have been presented in a paper submitted to ApJ Letters (Marengo et al., 2000c).

5.1 Imaging with mid-IR cameras

Ground-based mid-IR observations are limited by high background emission. Thermal emission from the atmosphere and telescope, at ambient temperature (300 K), is peaked at 10 μm. Photons coming from astronomical sources are then mixed with a background flux that can be orders of magnitude more intense. Special techniques have thus to be employed in order to separate the source signal from the background.

This section describes the beam switching technique we used for the background subtraction in our observations, and the limitations, in sensitivity and spatial resolution, which affects mid-IR imaging.

5.1.1 Observations in background-limited conditions

To maximize the efficiency of observations in high background conditions, and minimize the residual background induced noise, special telescopes have to be used. An optimal infrared telescope requires:

1. a long focal length, providing a small pupil beam. This is necessary to minimize the physical size of the detector, which needs to be refrigerated at low temperature (a few K) in order to maintain a high quantum efficiency and low noise.

2. aluminum coated mirrors, which minimize the thermal emission and the IR reflectivity

3. small secondary mirror support and light screen baffles, in order to reduce the emissions from any metal surface which is not essential

4. a small secondary mirror, with an oscillating support for sky emission subtraction.

The background emission subtraction is made with the *beam switching* technique illustrated in figure 5.1. Rapid beam switching is obtained by oscillating the secondary mirror of the telescope (*chopping*), in order to point alternatively the target source and the nearby sky. The chopping motion should be carried out at the frequency of a few hertz, above the dominant frequency of sky and detector fluctuations. Additional slow beam switching is made by moving the telescope (*nodding*) at a frequency of a few hundredth of hertz, to remove from the image the effects of different telescope collimation in the two chop beams.

The beam switching sequence consists of several steps (Hoffmann & Hora, 1999). First, the telescope is set to image the source in one of the chop beams, while the camera coadds frames into two separate buffers for the required integration time. One buffers contains the source plus background (frame A_+), the other only background, or background plus the source in a different position (frame A_-). Next, the telescope is nodded to a different sky position, and two more background images are obtained and stored in two additional buffers (frames B_+ and B_-). If the *throw* of the nodding is smaller than the detector field of view, then frames B_+ and B_- will contain images of the source in inverted positions with respect to the chopping A_+ and A_- frames. After the observation is complete, the telescope is returned to its original position, the four images individually stored, and then combined to provide a realtime image with the background subtracted:

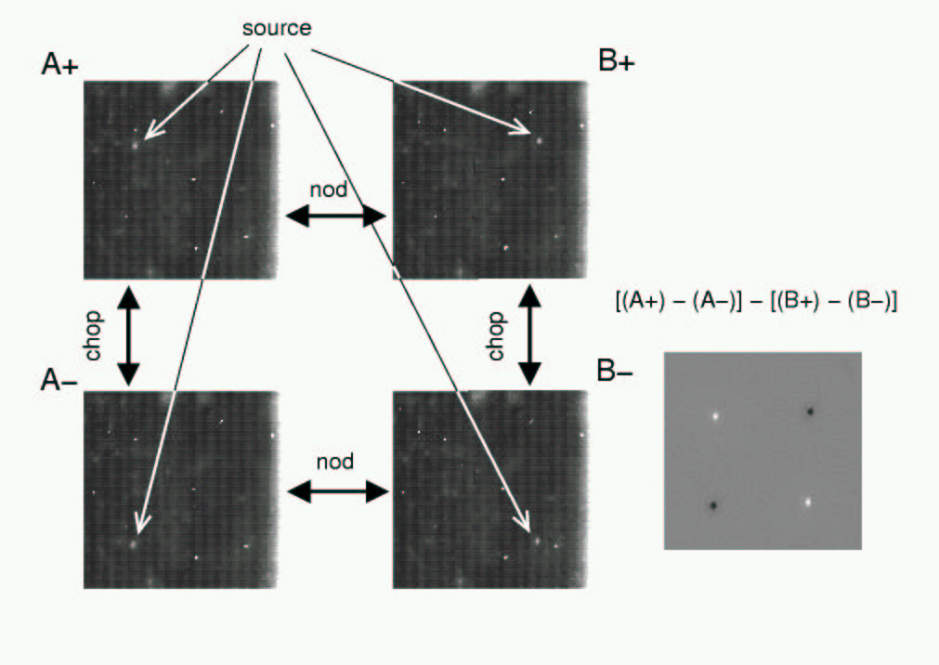

FIG. 5.1.— Schematic view of the beam switching technique for background subtraction in mid-IR imaging observations with the camera MIRAC3. The source is in all four beams.

$$\text{Image} = (A_+ - A_-) - (B_+ - B_-) \tag{5.1}$$

The total integration time on source is given by the combination of several parameters. If t_{ch} is the time during which the source is chopped in each nodding positions, and n_{nod} is the total number of nodding cycles in the observations, then:

$$t_{obs} = t_{ch} \cdot n_{nod} \cdot n_{beams} \tag{5.2}$$

where n_{beams} is the number of chop/nod beams in which the source is imaged inside the detector field of view ($n_{beams} = 4$ in figure 5.1 example). To estimate the total time required for the observation, one should take into account overheads due to the movements of the telescope from one nod position to the other, time wait to settle oscillation jitter of the chopping secondary, and readout time of the detector.

5.1.2 S/N ratio in background limited conditions

The total noise in the final image, expressed in "counts" of the analog to digital converters (A.D.U.) is given by different contributions:

N_R read-out noise, introduced by the A/D converters

$i_s \cdot t$ signal current noise, given by the fluctuations of the source signal "current" i_s

$i_{BG} \cdot t$ background current noise, residual of the background signal not perfectly subtracted with the beam switching technique

$i_{DC} \cdot t$ dark current noise, due to currents that are generated by the detector electronics even when the the shutter is closed to incident photons

$\epsilon(t)$ flat-field noise, associated to the relative efficiency of the individual detector elements (*pixels*). This noise, when the flux in a given pixel is above the linear regime, can be described by an exponential law with time $\epsilon(t) \sim e^t$.

Signal, background and dark current noise depend on the Poissonian statistics of the incident photons ($P_k = \langle i \cdot t \rangle / k!\, e^{-\langle i \cdot t \rangle}$); they are thus proportional to the square roots of the individual currents and frame time: $\sigma_k = \sqrt{\langle i \cdot t \rangle}$. The total noise for each detector pixel then is:

$$N = \sqrt{N_R^2 + i_s \cdot t + i_{BG} \cdot t + i_{DC} \cdot t + \epsilon(t)} \tag{5.3}$$

According to the dominant source of noise, the observation is said to be "read-out noise limited" ($N \sim R_N$), "photon-noise limited" ($N \sim \sqrt{i_s \cdot t}$), "background noise limited" ($N \sim \sqrt{i_{BG} \cdot t}$) and "flat-field" limited ($N \sim \sqrt{e^t}$). The signal to noise ratio of the image is:

$$\frac{S}{N} = \frac{i_s \cdot t}{\sqrt{N_R^2 + i_s \cdot t + i_{BG} \cdot t + i_{DC} \cdot t + \epsilon(t)}} \tag{5.4}$$

which assumes the following time dependence in the various regimes:

$$\frac{S}{N} \sim \begin{cases} t & \text{if "read-out noise limited"} \\ \sqrt{t} & \text{if "background-noise limited"} \\ \sqrt{t} & \text{if "photon-noise limited"} \\ t \cdot \sqrt{e^{-t}} & \text{if "flat-field limited"} \end{cases} \tag{5.5}$$

For mid-IR observations, since the background current is much greater than the source and dark currents, and the integration times are limited to avoid the exponential regime of the flat-field noise, the resulting S/N is dominated by the background. The total S/N of a mid-IR image is thus proportional to the square root of the total integration time.

5.1.3 Point Spread Function in the mid-IR

The spatial resolution achievable with a mid-IR camera depends on the optics of the telescope and the quality of the atmosphere surrounding the telescope. In ideal conditions, the image of a point source (i.e. an unresolved star) is given by a bi-dimensional Dirac δ-function. In a real system, the image observed on the focal plane of the detector is quite different, and is called *Point Spread Function*, or PSF.

The shape of the telescope and camera PSF is determined in part by diffraction, and in part by the atmospheric turbulence which deforms the wavefront of the stellar radiation.

The diffraction component can be derived by describing the the primary mirror as a circular aperture. The ideal diffraction limited PSF is then described by an Airy function:

$$F(x) = \left[2\frac{J_1(x)}{x}\right]^2, \qquad x = \frac{\pi\theta D}{\lambda} \tag{5.6}$$

where θ is the angular coordinate on the focal plane, λ the wavelength of the image and D the aperture of the telescope. In a real-life case, the presence of the secondary mirror and the camera secondary optics elements modify the standard Airy function to a more complex pattern. Deformations of the primary mirror due to different inclinations of the telescope, in absence of an active system able to compensate the non perfect rigidity of the system, can also change the shape of the ideal PSF. As a first approximation, equation 5.6 can be used to describe the PSF of an ideal system. In this case, the maximum angular resolution, given by the angular separation between the Airy function maximum and the first minimum, is:

$$\theta_{min}[\text{arcsec}] = 2.06 \cdot 10^5 \cdot 1.22\frac{\lambda}{D} \tag{5.7}$$

The PSF is also affected by the "blurring" induced by turbulence in the atmospheric layers between the source and the detector (*seeing*). Temperature gradients in the turbulent cells of the atmosphere produce variations Δn in the atmospheric refractive index. The variation $\Delta\mathcal{L}$ in the phase of

the source radiation wavefront are proportional to the cell size L and to the average number of cells along the optical path:

$$\Delta\mathcal{L} \simeq \sigma\sqrt{N} \cdot L \cdot \Delta n \tag{5.8}$$

If the telescope aperture D is small with respect to L, then the effect of seeing is to move around in the focal plane a point source PSF, according to the random oscillations of Δn. In large aperture telescopes, the image results from sampling a large fraction of the wavefront; the final PSF is thus projected in a fixed position, but enlarged to a size similar to the PSF displacement produced in a small aperture telescope. By reducing the observation time to the same scale of atmospheric cell fluctuations, one can "freeze" the position of the oscillating PSF, or minimize its deformation due to seeing.

The seeing PSF can be represented analytically by a gaussian. More elaborate functional approximations use a bi-parametric function, which describes the width of the central profile and the lateral wings (Moffat, 1969; King, 1971). The "wings" of the seeing PSF are usually approximated by an exponential.

In the analysis performed in the following sections, the shape of the PSF was derived by observing a standard star, assumed to be an unresolved point source. We also simulated a synthetic PSF profile, obtained by coadding a number of Airy functions randomly shifted to simulate the atmospheric seeing. The random displacement was set using a normalized gaussian random number generator, having zero median value and the required standard deviation to generate the seeing FWHM:

$$\delta(\theta) = C_n\, e^{-\theta^2/\sigma^2} \qquad \sigma = \frac{FWHM_{seeing}}{4\ln 2} \tag{5.9}$$

where C_n is a normalization constant.

In the visible, a medium aperture telescope provides a theoretical spatial resolution much higher than the seeing degradation of the image. In this case the observations are "seeing limited". In the mid-IR, on the contrary, the wavelength is 20 times longer, making the seeing less important. Typical mid-IR observations are thus "diffraction limited".

To have the correct spatial sampling of the instrumental PSF on the detector array, the magnification on the focal plane should be set to project the FWHM of the Point Spread Function on a matrix of 2×2 pixels (Nyquist criterium). These criteria fix the spatial scale on the array, which is thus decided by the aperture of the telescope.

5.2 Reduction of Mid-IR images

Mid-IR cameras usually store the collected data in some internal binary format, which has then to be converted to a format readable by the data reduction tools. This common file format is usually FITS (Flexible Image Transport System) (Wells et al., 1981; Greisen et al., 1981; Grøsbol et al., 1988; Harten et al., 1988).

Each camera has its own software to convert the stored data into FITS. In the case of TIRCAM and CAMIRAS this operation is performed by routines written in the IDL language by L. Corcione (Observatory of Torino, Italy) for TIRCAM and Philippe Galdemard (Service d'Astrophysique at Saclay, France) for CAMIRAS. The conversion of MIRAC3 data is instead performed by using the C program `mrc2fts` written by J.L Hora (Harvard-Smithsonian Center for Astrophysics, Cambridge MA) available at MIRAC web page `http://cfa-www.harvard.edu/~jhora/mirac/mirac.html`. At the same address the program `badcol` is also available, which corrects images that suffer from bad transmission of channels of data.

This section describes the data reduction pipeline adopted to process TIRCAM, CAMIRAS and MIRAC3 images, *after* their conversion to FITS format. It is assumed that the "positive" and "negative" chop-nod frames are already combined in the FITS files, as described in section 5.1.1.

The sequence which gives the single final image for each observation essentially consists of the following steps:

1. Determination of a bad pixel mask necessary to remove the contribution of individual unreliable detector pixels.

2. Flat field correction, which compensates for the different gains of the detector pixels.

3. Recentering of the individual frames in which the source integration has been splitted, shifting of the recentered frames with respect to the common centroid and coadding into a single image.

4. Photometric calibration of the final image, by using the observation of a reference star with known flux.

5. An optional further step consists in the deconvolution of the final image with a model PSF (usually derived from the image of a point source), in order to increase the spatial resolution.

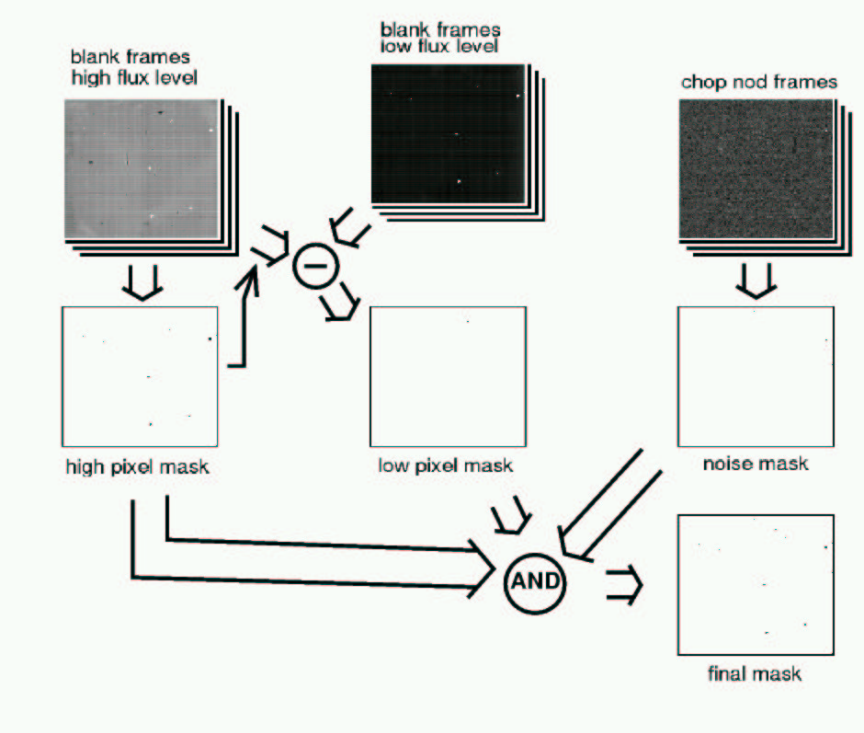

FIG. 5.2.— A bad pixel map is obtained from a set of individual frames in which the excessively high level, low level and high noise pixels are removed.

These operations have been performed on TIRCAM, CAMIRAS and MIRAC3 data with the aid of a specific package that I wrote in IDL, available at the MIRAC web page.

5.2.1 Masking bad pixels

The mask map specifies which image pixels should be combined in the final image from the single chop-nod frames. The reasons for which pixels have to be discarded are multiple:

1. Some pixels have an excessive dark current, which makes them appear like "hot spot" on the grabbed frames.

2. Other pixels are unresponsive, or suffer from vignetting of the pupil beam on the focal plane.

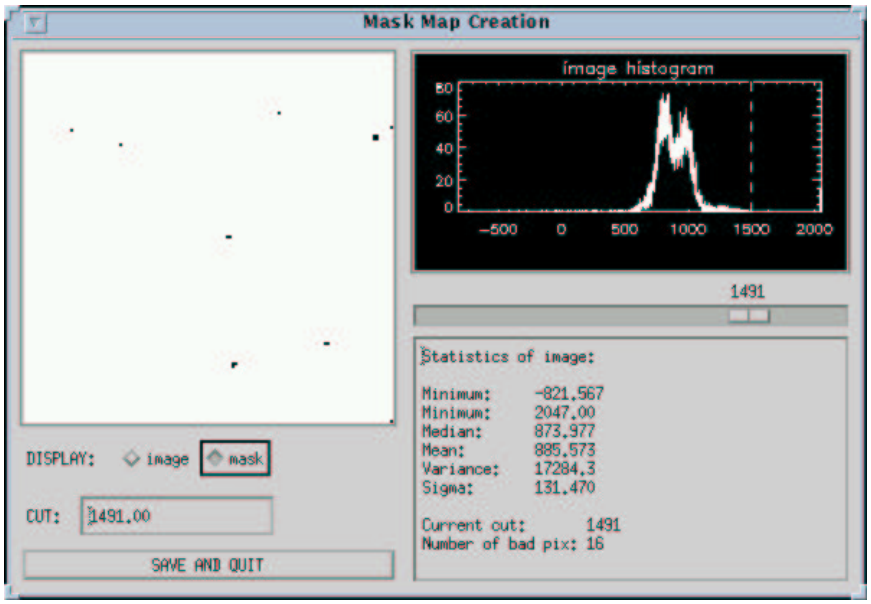

FIG. 5.3.— Screenshot of the `xmask_ima` IDL program used to create a bad pixel mask. The selection of pixels for the high level pixel map is shown.

3. Some pixels should be removed because they have high noise, outside the statistics of the whole array.

A pixel mask map is an image in which the rejected pixels are set to zero (off) value, and the good ones to unity (on). Each detector frame image can then be filtered by multiplication (logical `AND`) with the mask. As shown in figure 5.2, the following sequence allows the creation of a mask (Hoffmann et al., 1998):

1. A blanked image ("grab") at a standard frame time is used to select the pixels with unusual high flux, due to high dark current. The selected pixels constitute the "high level pixel mask".

2. The difference between a blank image at moderately high flux level, and a low flux blank image masked with the high level pixel mask, allows to exclude low flux pixels. This generates a "low level pixel mask".

3. The standard deviation of a set of nod-chop off-source images is computed pixel by pixel; pixels with unusual high σ are then set to zero in order to have a "noise pixel mask".

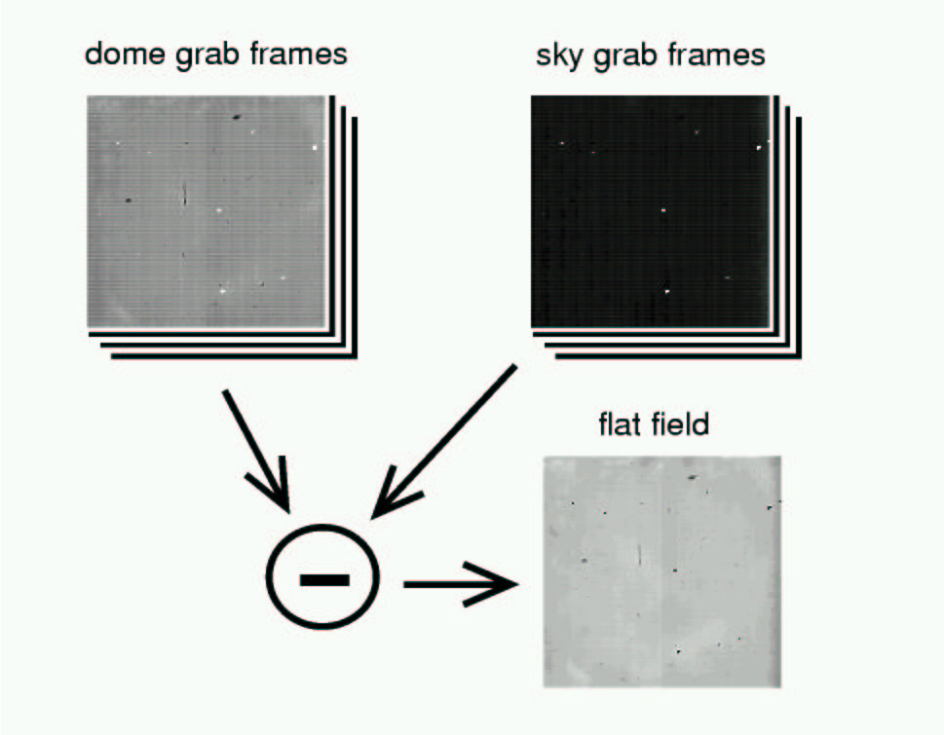

FIG. 5.4.— Process in which a flat field is derived. A sequence of low flux level frames is subtracted from a set of high flux level images. The result is normalized to unity.

4. The "high", "low" and "noise" masks are then combined in a single map, in which the "bad" pixels present in one of the intermediate masks are set to zero (logical `AND`).

The mask map used in the reduction of our data has been obtained with the aid of the IDL procedure `xmask_ima`, whose graphical user interface is shown in figure 5.3 while obtaining the high level pixel map.

5.2.2 Flat field correction

Each frame has what can be called a "zero-flux pattern" noise, that is the image obtained with zero luminous flux on the array, and with the same camera settings used during the real imaging. This pattern noise is introduced by the voltage offsets in the array and the signal processing electronics, and depends on the frame time because of the dark current. The pattern is also wavelength dependent, since the response of the detector pixels depends on

the frequency of the incident radiation. To obtain a useful image it is necessary to remove the zero flux pattern by using a "flat field" map. The corrected frame is given by dividing, pixel by pixel, the original image with the flat field.

There is no standard way to derive a flat field map in the mid-IR, but in general this operation involves the subtraction of several black frames obtained at two different flux levels. The procedure followed in our data reduction is described in figure 5.4 (Hoffmann et al., 1998):

1. A series of frames is taken by imaging the dome, without chopping or nodding. The frame integration time is chosen in order to avoid the saturation of the array. Due to the high emissivity of the dome (at ambient temperature) in the mid-IR, these constitute the required high flux level frames.

2. A second set of frames is taken, *without changing the orientation of the telescope*, by imaging a portion of empty sky (off-source frames, no chop or nod). This can be practically accomplished by opening the dome shutter, without moving the telescope after taking the dome frames. The frame integration time should be the same as before. Due to the lower emissivity of the sky, these constitutes the low flux level frames.

3. The two set of frames are separately median coadded, and then subtracted one from the other. The result is finally normalized to unity (each pixel is divided by the median level of the array).

5.2.3 Recentering and coadding individual frames

The final image for each observation is performed by coadding recentered single frames, flat filed corrected and bad pixel masked. We have done this operation with the aid of the custom written IDL procedure `xcenter_ima`, whose graphical user interface is shown in figure 5.5. The sequence of operations in which this is done is described in figure 5.6.

1. A set of chop-nod frames is initially corrected by using the appropriate flat field map.

2. The frames are rebinned on a sub-pixel grid (we used 5×5 pixels for each camera detector pixel, in order to increase the spatial sampling of the sources.

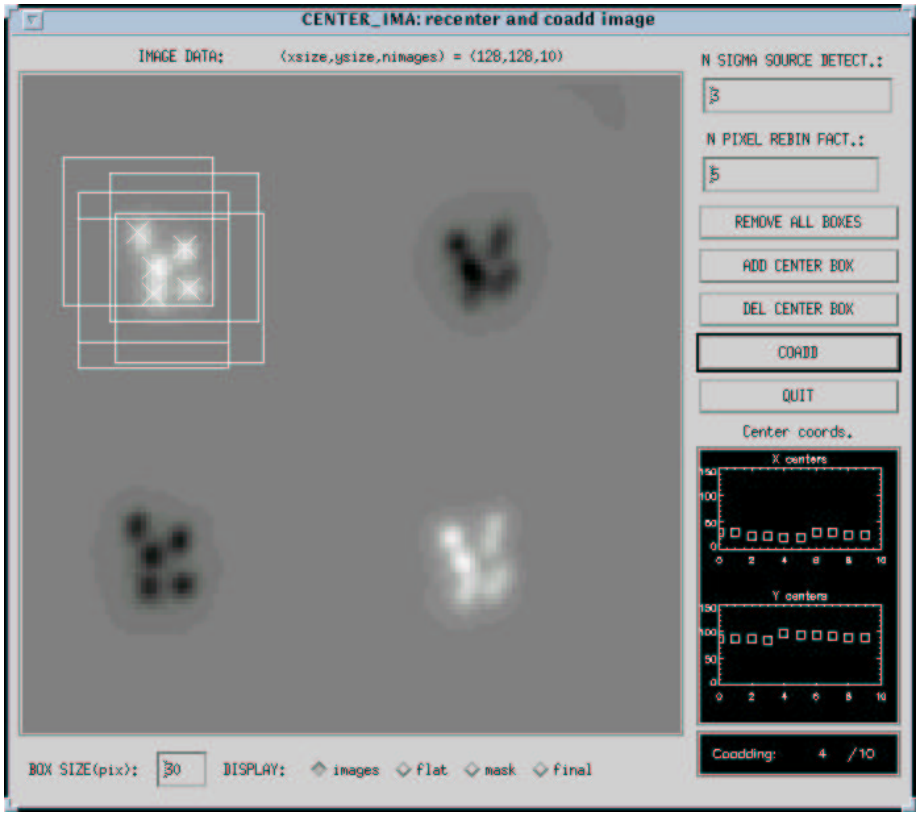

FIG. 5.5.— Screenshot of the `xcenter_ima` program, while performing the recentering of a set of chop-nod dithered observations. The display shows an un-recentered coadding of all frames, with the source in all four beams, and dithered in 5 positions in each beam. The crosses and boxes represent the hints of the user, entered with the cursor, for the position of the dithered source in the A+ beam. The source centroid coordinates are then computed inside each box, separately for each frame, by the recentering routine.

3. If the source was imaged in more than one chop-nod beam (as in figure 5.6, in which the source is in all four beams), the following steps should be performed for each beam which contains the source.

4. The coordinates of the source centroid are evaluated in each rebinned frame. This can be done computing the flux centroid of the source, by gaussian fitting, or by cross correlating the source brightness distribution in case of extended irregular sources.

5. The coordinates of each frame are recalculated in order to put the source centroid in a fixed position.

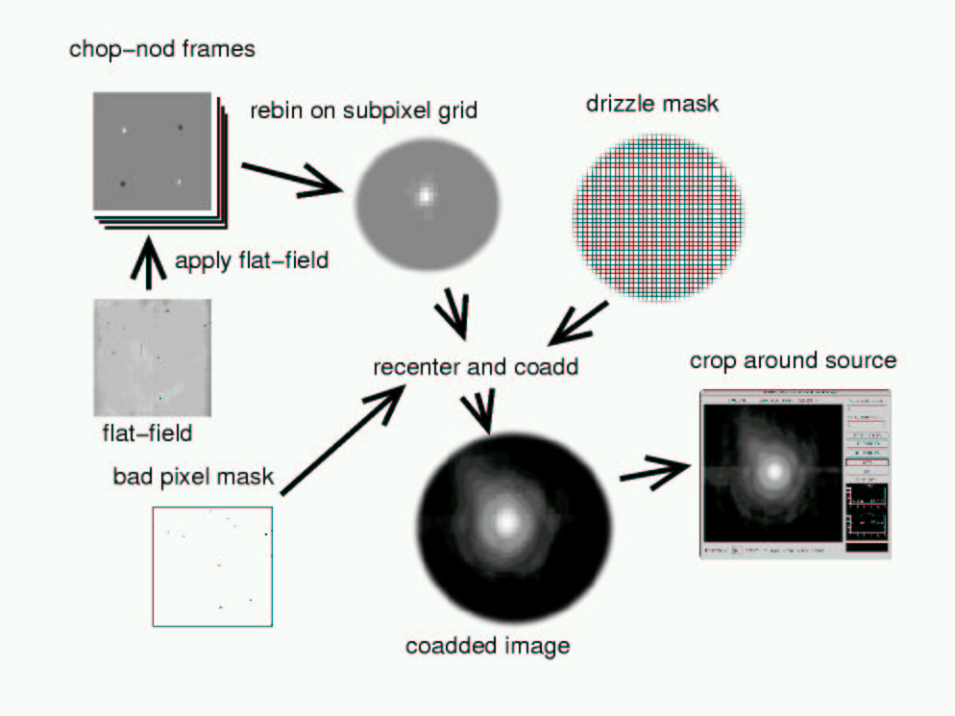

FIG. 5.6.— Steps in which a sequence of chop-nod observations are combined to produce a final image.

6. A rebinned bad pixel mask is associated to each frame, and shifted in the same way as the source frame.

7. An additional *drizzling mask* is added to the bad pixel mask (see below).

8. The source frames are coadded on the super-sampled grid, averaging the pixels with the same coordinate in the different frames. The average is computed by excluding the pixels masked-out by the bad pixel mask, and a weight can be associated to each frame, according to the square root of its integration time (to ensure uniform S/N ratio, see equation 5.5).

9. The final image is then cropped at the required size around the source.

If the source was observed in more than one beam, the single beam images are coadded together (provided that their recentering is the same). It is a good idea to weigh the coadd with respect to each image's S/N ratio.

This procedure ensures the flux normalization of the final image with respect to the single frame time. It also removes the effects of bad pixels in the final image, and provides a better spatial sampling of the source on the array. To maximize the efficiency of the spatial grid oversampling, the observations are usually made by dithering the source (with an offset of a few pixels) on the array, in order to project the image in different locations of the detector grid. To help the identification of the dithered source coordinates on the chop-nod frames, the `xcenter_ima` procedure allows cursor input on a preview of the coadded not recentered image (Figure 5.5).

The technique of *drizzling* can provide a better spatial resolution of the final image. Developed by Fructer & Hook (1998) to correct for the strong undersampling of the HST Wide Field Planetary Camera, it performs a coadding of rebinned frames without degrading the spatial resolution. The technique consists in "condensating" each detector pixel in a "*drop*", which occupies only a fraction of the original size of the detector pixel area projected on the super-sampled grid. This can be accomplished by masking out with a "drizzle mask" the sub-pixel grid columns and rows outside the required "drop" dimension, and then renormalizing the image to conserve the flux (see figure 5.6). We found the drizzling technique effective in improving the source spatial resolution when performed on a very large number of individual frames ($\gtrsim 250$), to ensure an uniform coverage of the image on the sub-pixel grid. This condition is typically met in our "fast mode" technique experimented with the camera MIRAC3 at IRTF.

5.2.4 Photometric calibration

The photometric calibration of the final images was made with the procedure `xphot_ima` whose graphical user interface is shown in figure 5.7. The program computes aperture photometry for each source by calibrating the final image with a reference star of known photometry, observed immediately before and after the source.

The aperture photometry is done in a similar fashion to the IRAF package `DAOPHOT` (Stetson, 1987). For both source and reference the user provides the aperture radius and the inner and outer radii of an annulus in which the sky emission level is estimated. The program computes the source counts as the difference between the counts in the source aperture, and the sky annulus, of equivalent aperture area:

$$counts = counts_{aper} - counts_{sky} \cdot \frac{A_{aper}}{A_{sky}} \tag{5.10}$$

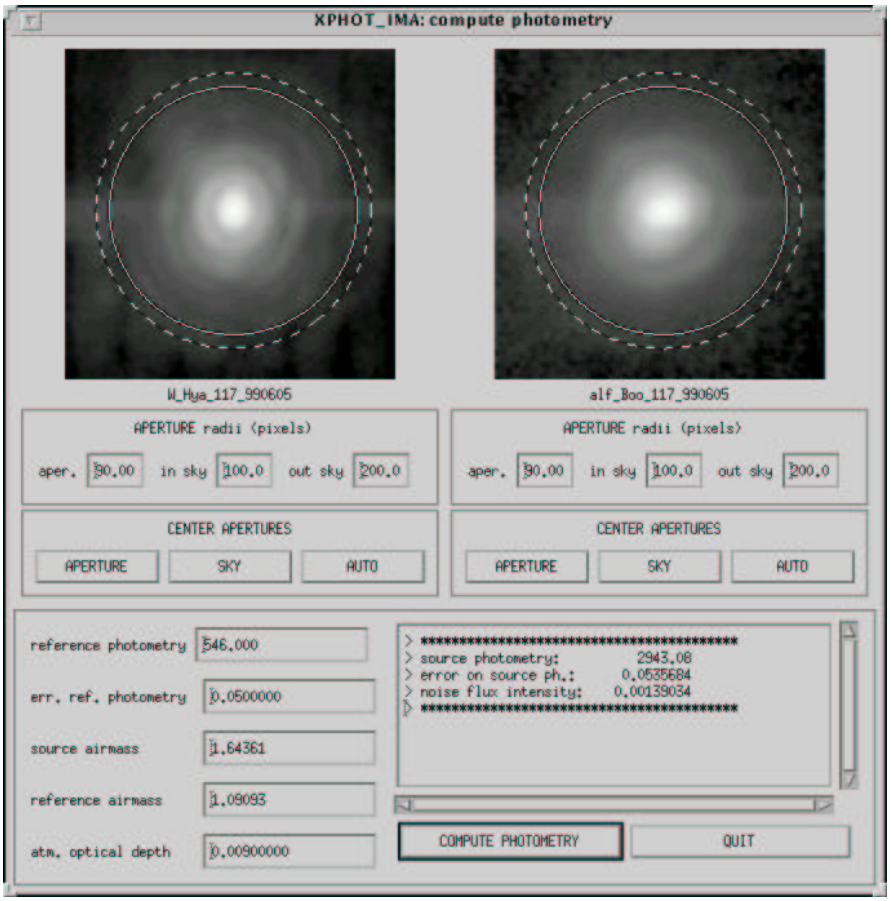

FIG. 5.7.— Screenshot of the `xphot_ima` program, while computing the photometry of the SR AGB source W Hya. The source was observed with MIRAC3 in June 1999, with α Boo as photometric reference star. The aperture is identical for source and reference, and centered with the source and reference image. The sky annulus radius starts at the dashed circle, and ends outside the border of the two images. The coordinates and radii are given in units of the rebinned super-sampled image (1 pixel = 1/5 MIRAC3 pixels).

The calibration factor is the ratio between the reference star photometry and counts. The airmass correction is then computed from the ratio of the air mass of source and reference at the time of their respective observations:

$$f_{air} = e^{-\tau_{air} \cdot \frac{air_{source}}{air_{ref}}} \tag{5.11}$$

where the optical depth of the atmosphere is given (for our standard photometric system) in figure 3.7.

The source photometry is then measured by dividing the source counts with the calibration factor, and multiplying the result with the airmass correction.

The error of each measurement is computed as the geometric sum of the standard deviation of sky values in source and reference frames, the uncertainty in the mean sky brightness, and the relative error in the reference star photometry. The random photon noise in the source and reference image is not considered, since the major contributions to the total errors in mid-IR background limited conditions are due to the residual background noise (see equation 5.5).

5.2.5 Deconvolution techniques

Sources showing extended emission were deconvolved with the PSF, in order to achieve a better angular resolution. As explained in section 5.1.3, distortion of the source radiation while crossing the atmosphere and the telescope-camera optics degrade the spatial resolution of the image, and the image of a generic point source is spread into a PSF figure. The generic radial brightness profile $F_\nu(\theta)$ is thus imaged on the detector focal plane as the enlarged profile $F'_\nu(\theta)$:

$$F'_\nu(\vec{\theta}) = \int F_\nu(\vec{\theta'})\, PSF(\vec{\theta} - \vec{\theta'})\, \mathrm{d}\vec{\theta'} \tag{5.12}$$

If the shape of the PSF is known, it is in principle possible to attempt a deconvolution to reverse the image degradation. This operation, however, does not yield a unique solution. Several methods have thus been developed to compute the "most likely" deconvolved source image.

In section 5.4 we have tested two deconvolution procedures on all the observed sources, by using the (photometric) reference source as a model for the real PSF. This approach has its own limitations, mainly because of the instability of the real PSF, whose shape is sensitive to several factors:

- the telescope orientation (the telescope deforms under its own weight, and the deformation depends on its position)
- the seeing and the presence of wind
- the ambient temperature, which changes the distance between the primary and secondary mirror
- the focus of the camera and the distance of the image from the optical axis

In order to limit these complications, we made an effort to observe the reference stars as close as possible, in time and sky orientation, to the relative source. The absence of a reasonable number of bright infrared standards, however, makes this procedure relatively difficult.

The deconvolutions were made with two different algorithms, *maximum entropy* based on Hollis et al. (1992) and *maximum likelihood* based on Richardson (1972) and Lucy (1974). We applied both methods on each extended source, and the final results were then compared, to reduce the possibility of spurious detection in the deconvolved images.

5.3 Mid-IR colors of AGB circumstellar envelopes

This section describes the observational campaign carried on with the mid-IR cameras TIRCAM and CAMIRAS, aimed to collect images and photometry of AGB circumstellar envelopes.

The results of the observations are reviewed, and used as an observational test for the diagnostic tools developed in chapter 3, in preparation of the more extended imaging campaign described in section 5.4.

5.3.1 The cameras TIRCAM and CAMIRAS

The camera TIRCAM has been developed in a collaboration between the "Istituto di Astrofisica Spaziale" of the Italian National Research Council (C.N.R. Rome), the Astronomical Observatory of Torino (Italy) and the "Dipartimento di Fisica Generale" of the University of Torino (Italy). The camera is described in Persi et al. (1994), and at the time of the observational campaign was equipped with a 10×64 pixels Si:As array detector built by the Huges Aircraft Corporation (USA). The pixel scale of the array was 1.23"/pix and 1.38"/pix at TIRGO and SPM respectively. The photometric system of the camera included the full set of 10% passband filters described in section 3.3.1.

The camera CAMIRAS, developed at the Service d'Astrophysique at Saclay, France (Lagage, P.O., 1992), was equipped with a 192×128 Si:Ga/DVR array detector. The available photometric system was similar to the one of TIRCAM, and we performed our observations with the 10% filters having effective wavelength of 8.55, 9.56, 11.21, 12,45 and 16.64 μm. To maximize the S/N and reduce the total observation time, we performed most of the observations with the source in all four chop-nod beams. The pixel scale of CAMIRAS at TIRGO was 0.72"/pix.

Table 5.1 TIRCAM/CAMIRAS AGB sources

#	Source	Class	IRAS	LRS[a]	Var. type[b]
1	KU And	O-rich	00042+4248	26	M
2	WX Psc	O-rich	01037+1219	4n	M
3	W And	S-star	02143+4404	22	M
4	*o* Cet	O-rich	02168−0312	2n	M
5	AFGL 618	C-rich	04395+3601	62	–
6	IRAS 06088+1909	C-rich	06088+1909	–	–
7	Red Rect	C-rich	06176−1036	80	–
8	IRC+40156	O-rich	06297+4045	27	–
9	X CnC	C-rich	08525+1725	42	SRb
10	R LMi	O-rich	09425+3444	24	M
11	R Leo	O-rich	09448+1139	1n	M
12	IRC+10216	C-rich	09452+1330	43	M
13	CIT 6	C-rich	10131+3049	04	SRa
14	Y CVn	C-rich	12427+4542	42	SRb
15	RT Vir	O-rich	13001+0527	21	SRb
16	S CrB	O-rich	15193+3132	24	M
17	WX Ser	O-rich	15255+1944	29	M
18	V CrB	C-rich	15477+3943	4n	M
19	U Her	O-rich	16235+1900	23	M
20	NSV 9118	O-rich	17297+1747	14	SR
21	AFGL 2205	O-rich	18348−0526	3n	M
22	NSV 11225	C-rich	18397+1738	43	–
23	CRL 3068	C-rich	23166+1655	02	–

[a] LRS class from Loup et al. (1993).
[b] Variability type derived from GCVS (Kopolov et al., 1998).

5.3.2 Observations

The target list was selected according to the mid-IR brightness and estimated distance of the sources, to maximize the S/N ratio and possibly detect extended emission from the dust in the AGB envelopes.

Table 5.1 shows the list of the observed sources. For each source is indicated the chemical type, the IRAS name and LRS class, and the variability

Table 5.2 Photometry of TIRCAM sources

#[a]	Source	$F_{8.8}$ [Jy]	$F_{9.8}$ [Jy]	$F_{11.7}$ [Jy]	$F_{12.5}$ [Jy]	epoch
3	W And	97	-	143	205	Dec 93
4a	*o* Cet	3730	3670	4650	2650	Oct 92
4b	*o* Cet	2100	3330	3540	1780	Dec 93
5	AFGL 618	141	188	275	302	Dec 93
9	X CnC	107	151	40	-	Dec 93
10	R LMi	331	377	409	268	Dec 93
11	R Leo	1780	1700	2780	1860	Dec 93
12	IRC+10216	28300	33100	37100	37200	Dec 93
14	Y CVn	254	198	283	259	May 93
15	RT Vir	369	468	556	325	May 93
16	S CrB	183	187	224	134	May 93
17	WX Ser	116	206	86	-	May 93
18	V CrB	103	225	129	105	May 93
19	U Her	547	619	553	403	May 93
21	AFGL 2205	133	-	340	656	May 93
22	NSV 11225	782	792	899	810	May 93

[a] List number given according to table 5.1

type. The sample consists of 23 objects of which 12 O-rich, 10 C-rich and 1 S-star. Two sources are post-AGB (AFGL 618 and AFGL 2205), two are pre-PN (Red Rectangle and CRL 3068) and the others are in the AGB phase.

TIRCAM observations were performed in 1992 and 1993 at the 1.5 m italian "Telescopio InfraRosso al GornerGrat" (TIRGO) and at the 2.1 m infrared telescope of the Observatorio Astronomico National (Mexico) at San Pedro Martir (SPM), Baja California.

The camera used a set of 10% filters centered at 8.8 (continuum + PAH), 9.8 (main silicate feature), 11.7 (SiC + PAH) and 12.5 (continuum + PAH) μm. The data reduction was performed using IRAF, MIDAS and IDL packages, as described in section 5.2. The effective integration times were ranging from 10 sec to 5 min, according to the source brightness. The sources were imaged in one beam, due to the small size of the detector.

The measured photometry of the observed sources is listed in table 5.2. The photometric calibration was achieved by observing repeatedly the standard stars α Boo and α Tau. The zero point estimates show an uncertainty of about 5%; the nominal errors of the data in the table 5.2 (1σ) are $\lesssim$7% in the 8.8 and 9.8 μm filters, and $\lesssim$15% in the other two.

The data in table 5.2 was originally published in Busso et al. (1996),

Table 5.3 Photometry of CAMIRAS sources and standards

#[a]	Source	$F_{8.55}$ [Jy]	$F_{8.57}$ [Jy]	$F_{9.56}$ [Jy]	$F_{11.21}$ [Jy]	$F_{12.24}$ [Jy]	$F_{12.45}$ [Jy]	$F_{16.64}$ [Jy]	epoch
1	KU And	488	433	763	1030	-	497	-	Nov 96
2	WX Psc	846	702	1050	1040	-	364	863	Nov 96
3	W And	154	151	188	162	-	115	-	Nov 96
5a	AFGL 618	226	192	322	378	413	484	882	Nov 96
5b		-	-	272	-	559	-	-	Feb 97
6	06088+1909	40	-	37	42	-	37	-	Nov 96
7	Red Rectangle	235	-	937	-	-	-	3030	Feb 97
8	IRC+40156	-	54	-	76	50	-	-	Nov 96
13	CIT 6	-	-	-	3880	3070	-	1930	Feb 97
20	NSV 9118	221	-	283	222	290	-	-	Feb 97
23	CRL 3068	288	-	362	404	-	472	280	Nov 96
std	α Aur	326	325	262	191	161	156	88	
std	α Tau	838	834	682	509	433	420	246	
std	β And	354	352	286	212	179	174	100	
std	β Gem	170	169	136	99	84	81	46	
std	β Peg	524	522	429	323	276	268	159	

[a] List number given according to table 5.1; std indicates photometric standards.

where the photometry of the C-rich source FX Ser was also given. This measurement was subsequently rejected (Marengo et al., 1999), due to the presence of vignetting in the original images.

An additional number of 10 sources was observed with the camera CAMIRAS during two observing runs at TIRGO in November 1996 and February 1997. These observations were made with a set of 10% passband filters centered at 8.55, 9.56, 11.21, 12.45 and 16.65 μm, plus narrow band filters at 8.57 and 12.24 μm. The total integration time ranged between 5 and 15 minutes, according to the source brightness. The sources were observed in all four beams with a chop-nod throw of 20", in order to maximize the source S/N.

The standard stars α Aur, α Tau, β And, β Gem and β Peg were observed to calibrate the images and derive the point-spread function (PSF). The calibration fluxes in the CAMIRAS photometric system were derived for each standard in a two step process: (1) a synthetic spectrum for each star was constructed by fitting available IR photometry data (Gezari, 1993) with the Engelke + SiO modified black body described in section 3.2.2, and (2) convolved with the CAMIRAS filter profiles to provide the flux at each wavelength. The reference fluxes computed with this procedure are listed in

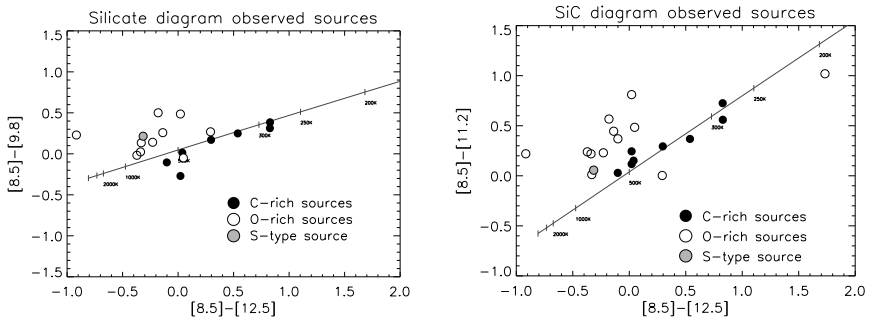

FIG. 5.8.— Silicate and SiC color diagram of TIRCAM/CAMIRAS sources. C-rich envelopes are filled circles, O-rich are empty and the S-star is grey.

table 5.3. The observed PSF were dependent on the local seeing conditions, varying from night to night. The mean value of the PSF FWHM was ~ 2.2" at 8.55 μm and ~ 3" at 12.45 μm.

Table 5.3 reports the integrated flux densities of CAMIRAS sources, already published in Marengo et al. (1999). The photometric statistical error (comprehensive of the calibration errors) is approximately 10%. Of all the sources in table 5.3, only WX Psc, IRC+10216, CRL 3068 and Red Rectangle appear to be spatially resolved (within our measured PSF) in at least one filter.

5.3.3 Mid-IR colors and mass loss

The affinity of TIRCAM and CAMIRAS filters with the "standard" photometric system introduced in section 3.3.1 allows an observational test of the color diagrams previously defined. A color correction to the measured photometry is in principle required to reconcile the small differences between CAMIRAS and TIRCAM set of filters, and the "standard" ones. This color correction was thus estimated by convolving the filters profile with the IRAS spectra of AGB stars with different LRS class. The values thus obtained, however, turned out to be much smaller than the uncertainty of the measurements in our photometry, and have therefore been ignored. For this reason we consider equivalent CAMIRAS 8.55 and 9.56 filters with TIRCAM 8.5 ans 9.8 μm fluxes.

The "silicate" and "SiC" feature color color diagram of the observed sources are plotted in figure 5.8. They confirm the results found in chapter 3, with C-rich sources along the black body, and [optically thin] O-rich envelopes in the upper part of the diagrams.

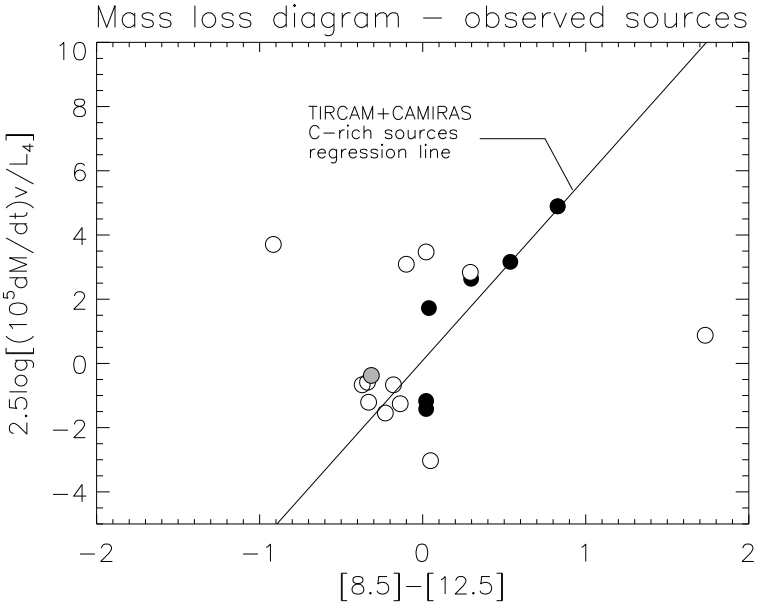

FIG. 5.9.— The mass loss parameter vs. mid-IR "continuum" color for TIRCAM/CAMIRAS sources. A regression line for C-rich sources is computed and drawn on the diagram.

One or more estimates for mass loss rate, bolometric flux, envelope outflow velocity and total luminosity are available in Loup et al. (1993) for 21 of the observed sources, and are listed in table 5.4. These values allow to compute the mass loss parameter defined in section 3.3.5, which we found related to the infrared continuum color [8.5]-[12.5]. The validity of this correlation can be tested by using MIRAC/CAMIRAS photometry for the observed sources.

Figure 5.9 shows the color - mass loss diagram for the observed sample. The plot uses the photometry listed in table 5.2 and 5.3. The mass loss parameter is derived from table 5.4 (the average value is computed for sources with multiple estimates of $\dot{M}$ and L).

The main difference with the similar plot in figure 3.13 is the much lower dispersion of the sources with respect to the mass loss parameter. C-rich sources, in particular, appear to be on a sequence, which is plotted on the diagram. A comparison with figure 3.13 shows that the regression line found for C-rich TIRCAM/CAMIRAS sources defines a lower boundary of the region populated by L93 (Loup et al., 1993) C-rich sources. This is a

TABLE 5.4 PHYSICAL PARAMETERS OF TIRCAM/CAMIRAS AGB SOURCES

#	Source	$4\pi \cdot 1\mathrm{kpc}^2 F_{total}$ $L_\odot$	$\dot{M}$ [$\mathrm{M_\odot\ yr^{-1}}$]	v_e [$\mathrm{km\ s^{-1}}$]	d [kpc]	L [$\mathrm{L_\odot}$]
1	KU And	$1.5 \cdot 10^4$	$9.7 \cdot 10^{-6}$	21.7	0.82	$1.0 \cdot 10^4$
			$2.4 \cdot 10^{-5}$	21.7	1.10	$1.8 \cdot 10^4$
2	WX Psc	$3.4 \cdot 10^4$	$8.5 \cdot 10^{-6}$	20.7	0.54	$9.9 \cdot 10^3$
			$1.2 \cdot 10^{-5}$	20.7	0.51	$8.8 \cdot 10^3$
			$2.4 \cdot 10^{-5}$	20.7	0.51	$8.8 \cdot 10^3$
3	W And	$4.4 \cdot 10^4$	$8.0 \cdot 10^{-7}$	10.7	0.48	$1.0 \cdot 10^3$
			$9.7 \cdot 10^{-7}$	10.7	0.63	$1.7 \cdot 10^3$
4	*o* Cet	$8.1 \cdot 10^5$	$5.0 \cdot 10^{-7}$	5.6	0.11	$9.8 \cdot 10^3$
			$5.7 \cdot 10^{-7}$	5.6	0.08	$5.1 \cdot 10^3$
			$1.0 \cdot 10^{-6}$	5.6	0.08	$5.1 \cdot 10^3$
			$1.0 \cdot 10^{-7}$	5.6	0.08	$5.1 \cdot 10^3$
			$2.1 \cdot 10^{-6}$	5.6	0.08	$5.1 \cdot 10^3$
5	RAFGL 618	$7.8 \cdot 10^3$	$6.7 \cdot 10^{-5}$	19.5	1.30	$1.3 \cdot 10^4$
			$5.6 \cdot 10^{-5}$	19.5	1.30	$1.7 \cdot 10^4$
6	IRAS 06088+1909	–	–	–	–	–
7	Red Rect	–	–	–	–	–
8	IRC+40156	$3.7 \cdot 10^3$	$1.0 \cdot 10^{-5}$	16.3	1.60	$9.5 \cdot 10^3$
9	X CnC	$2.1 \cdot 10^4$	$7.7 \cdot 10^{-7}$	9.7	0.69	$1.0 \cdot 10^4$
			$4.6 \cdot 10^{-7}$	9.7	0.64	$8.6 \cdot 10^3$
10	R LMi	$9.4 \cdot 10^4$	$2.8 \cdot 10^{-7}$	7.0	0.33	$1.0 \cdot 10^4$
			$5.0 \cdot 10^{-7}$	7.0	0.35	$1.2 \cdot 10^4$
11	R Leo	$5.0 \cdot 10^5$	$1.0 \cdot 10^{-7}$	8.5	0.14	$9.8 \cdot 10^3$
			$8.0 \cdot 10^{-8}$	8.5	0.30	$4.5 \cdot 10^4$
			$6.0 \cdot 10^{-7}$	8.5	0.24	$2.9 \cdot 10^4$
12	CW Leo	$6.6 \cdot 10^5$	$4.8 \cdot 10^{-5}$	14.7	0.29	$5.6 \cdot 10^4$
			$2.2 \cdot 10^{-5}$	14.7	0.22	$5.6 \cdot 10^4$
13	CIT 6	$6.9 \cdot 10^4$	$6.0 \cdot 10^{-6}$	16.8	0.38	$1.0 \cdot 10^4$
			$2.6 \cdot 10^{-6}$	16.8	0.19	$2.5 \cdot 10^3$
			$4.8 \cdot 10^{-6}$	16.8	0.39	$1.0 \cdot 10^4$
			$7.5 \cdot 10^{-6}$	16.8	0.48	$1.6 \cdot 10^4$
14	Y CVn	$8.7 \cdot 10^4$	$4.2 \cdot 10^{-7}$	8.2	0.34	$1.0 \cdot 10^4$
			$2.8 \cdot 10^{-7}$	8.2	0.35	$1.1 \cdot 10^4$
			$1.4 \cdot 10^{-6}$	8.2	0.35	$1.1 \cdot 10^4$
			$1.2 \cdot 10^{-7}$	8.2	0.41	$1.5 \cdot 10^4$
15	RT Vir	$1.3 \cdot 10^5$	$7.4 \cdot 10^{-7}$	9.3	0.28	$1.0 \cdot 10^4$
			$1.3 \cdot 10^{-6}$	9.3	0.97	$1.2 \cdot 10^5$
			$6.0 \cdot 10^{-6}$	9.3	1.00	$1.3 \cdot 10^5$
			$4.9 \cdot 10^{-7}$	9.3	0.32	$1.3 \cdot 10^4$
16	S CrB	$2.3 \cdot 10^4$	$5.8 \cdot 10^{-7}$	6.3	0.66	$1.0 \cdot 10^4$
			$6.0 \cdot 10^{-7}$	6.3	0.42	$4.1 \cdot 10^3$
17	WX Ser	$7.2 \cdot 10^3$	$2.6 \cdot 10^{-6}$	8.8	1.20	$1.0 \cdot 10^3$
			$5.3 \cdot 10^{-7}$	8.8	0.72	$3.7 \cdot 10^3$
18	V CrB	$1.5 \cdot 10^4$	$5.2 \cdot 10^{-7}$	7.8	0.82	$1.0 \cdot 10^4$
			$5.8 \cdot 10^{-7}$	7.8	1.02	$1.6 \cdot 10^4$
19	U Her	$3.2 \cdot 10^5$	$2.6 \cdot 10^{-7}$	13.1	0.18	$1.0 \cdot 10^4$

Table 5.4: continue.

#	Source	$4\pi \cdot 1\mathrm{kpc}^2 F_{total}$ $L_\odot$	$\dot{M}$ [$M_\odot$ yr^{-1}]	v_e [km s^{-1}]	d [kpc]	L [$L_\odot$]
20	NSV 9118	$1.6 \cdot 10^4$	$9.7 \cdot 10^{-6}$	16.3	0.79	$1.0 \cdot 10^4$
			$2.0 \cdot 10^{-5}$	16.3	1.20	$2.3 \cdot 10^4$
			$1.6 \cdot 10^{-5}$	16.3	1.20	$2.3 \cdot 10^4$
21	AFGL 2205	$1.1 \cdot 10^4$	$2.1 \cdot 10^{-6}$	10.6	0.95	$9.9 \cdot 10^4$
22	NSV 11225	$2.8 \cdot 10^4$	$3.8 \cdot 10^{-6}$	14.2	0.60	$1.0 \cdot 10^4$
			$9.1 \cdot 10^{-6}$	14.2	0.79	$1.7 \cdot 10^4$
			$2.4 \cdot 10^{-6}$	14.2	0.79	$1.7 \cdot 10^4$
			$6.0 \cdot 10^{-6}$	14.2	0.64	$1.1 \cdot 10^4$
23	CRL 3068	$1.1 \cdot 10^4$	$8.4 \cdot 10^{-6}$	14.1	0.95	$9.9 \cdot 10^3$
			$6.4 \cdot 10^{-6}$	14.1	0.57	$3.6 \cdot 10^3$
			$1.2 \cdot 10^{-5}$	14.1	1.00	$1.1 \cdot 10^4$
			$2.1 \cdot 10^{-5}$	14.1	1.04	$1.2 \cdot 10^4$

consequence of the selection process in which the targets to be observed were chosen. In order to maximize the S/N ratio available with TIRCAM and CAMIRAS detectors, we have selected the brightest sources with the largest infrared excess available: in the case of the C-rich envelopes this favored the sources in the lower boundary of the color distribution, that is where the infrared excess is maximum. O-rich sources, on the contrary, are spread on the whole diagram.

5.3.4 One example of extended source: WX Psc

The limited aperture of TIRGO and SPM telescopes does not allow the necessary angular resolution to spatially resolve AGB circumstellar envelopes. The collected images were however analyzed to search for extended emission beyond the instrumental PSF. Figure 5.10 shows the image of the bright O-rich source WX Psc (alias CIT3) at 8.8 μm, which represents the best candidate for spatial extension among CAMIRAS sources.

This source has been recently observed at 11.5 μm at the Wyoming Infrared Observatory (Sudol et al., 1999), where the visibility curve in the E-W direction was derived, and no extension was found (leading to the conclusion that at that wavelength the circumstellar shell should have an angular diameter of 0.63" or less). Similarly, a far-IR search (60 and 100 μm) in the IRAS database conducted by Young et al. (1993) was not able to resolve extended emission from the source.

Near-IR speckle observations at the SAO 6m telescope (Irrgang et al, 1998), were able to identify two separate components in the circumstellar

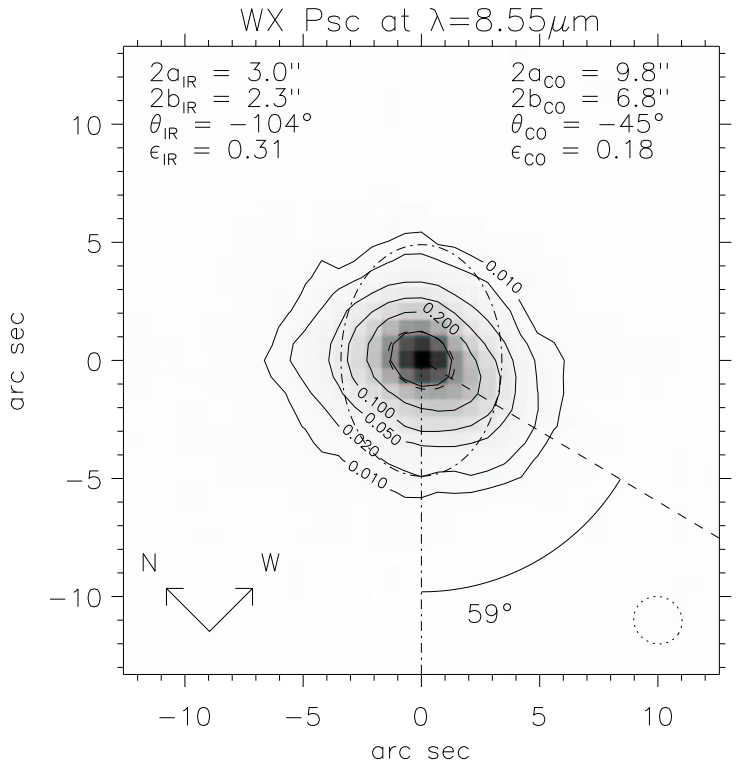

FIG. 5.10.— Images and contour plots of the O-rich AGB envelope WX Psc at 8.55 μm. Contour levels are shown at 0.01, 0.02, 0.05, 0.1, 0.2 and 0.5 of the source maximum, where the 0.01 contour corresponds to the 5σ noise level. The source radial brightness distribution is fitted with a 2D elliptical gaussian whose major and minor axis, orientation (from E direction, clockwise) and asymmetry are indicated in the left column. The "sizes" a and b of the interpolating elliptical gaussian are related to the FWHM by the relation FWHM = size $\cdot\sqrt{2\ln 2}$. The dashed contour and line are the half maximum ellipse of the fitting gaussian and the orientation of its major axis. The dot dashed contour and line indicate the size and orientation of the secondary gaussian component of the CO(J=1→0) emission as measured by Neri et al. (1998). The parameters of the CO fitting are indicated in the right column for comparison; note the 59° rotation between the orientation of the IR and the CO major axis. The dotted circle in the lower right corner is the beam size of the PSF, derived from the half maximum contour of a standard star.

envelope of the source, consisting of a partially resolved smaller structure (representing the innermost region of the envelope) and a fully resolved extended nebulosity that "[...] *might point to a change of the physical properties in the outflow*".

High resolution ^{12}CO (J=1→0) and (J=2→1) maps of the O-rich source have been obtained using radio interferometers able to resolve the molecular envelope of this object. In Neri et al. (1998), IRAM observations of WX Psc are fitted by using a double component envelope in which the primary component (of size ∼30") is spherical, and the secondary elliptical, with asymmetry $\epsilon_{CO} = 0.18$ (major and minor sizes 9.8" and 6.8") and major axis rotated by 45° from E to S.

We have attempted a similar 2D gaussian fit on our 8.55 μm image (not deconvolved with the PSF), and the results are shown in figure 5.10. The best fit parameters indicate an elongated shape (major and minor size of 3.0" and 2.3" respectively) with asymmetry $\epsilon_{IR} = 0.31$, oriented with the major axis at 104° from the E direction (counterclockwise). The comparison of the source image with the PSF derived from nearby standard stars (symmetrical and with FWHM of about 2.0"), implies an extension of WX Psc in the N-S direction, while the source remains unresolved along the E-W axis (in agreement with Sudol et al. (1999) observation). The extension of the source is less clear in our images at longer wavelengths.

The smaller dimensions of the mid-IR image, compared to the CO map, its larger asymmetry and the different orientation (59° rotation between the CO and IR envelope) suggest the possibility that the mid-IR and the CO observations refer to physically distinct regions of the envelope. This consideration, together with the failure to detect an extended dust emission at 60 and 100 μm, leads to the conclusion that in the envelope of WX Psc the dust appears to be concentrated only in the central regions. This further suggests that dust is condensed close to the photosphere of WX Psc, in a non spherical environment. At larger distances from the central star the dust is undetectable. The progressive decrease in the envelope asymmetry probed by the CO observations can be explained either assuming a disk-like geometry in the dust spatial distribution or, alternatively, assuming an axisymmetrical circumstellar envelope that becomes more and more spherical as it expands with the AGB wind.

The spatial resolution of our image does not help to clarify the underlying geometry of the source, but brings into evidence that even with a small aperture telescope it is possible to derive information on the spatial distribution of dust for some bright and close-by objects. A larger telescope and a more sensitive camera is a necessary step to confirm this observations and

collect extended images for a larger sample of sources. An observational effort of this nature is described in the next section.

5.4 MIRAC imaging of extended AGB envelopes

The mid-IR camera MIRAC has been successfully operated in imaging projects devoted to advanced stages of stellar evolution, such as PN, pre-PN and post-AGB stars (Hora et al. 1990, 1993, 1996, Dayal et al. 1998, Meixner et al. 1999). These evolved objects constitute an ideal target for the camera, due to their strong infrared emission and large physical size. The strong departures from spherical symmetry already observed in high resolution optical and near-IR observations (see, e.g the HST "gallery" of PN and pre-PN) are confirmed in MIRAC images mapping the spatial distribution of the circumstellar dust.

AGB circumstellar envelopes are a greater challenge for the current state of mid-IR imaging. This is the consequence of many factors:

- post-AGB, pre-PN and PN have in general larger angular sizes than AGB circumstellar envelopes, which are a more difficult target for telescopes of median aperture.

- a dramatic increase in the mass loss rate is characteristic of the transition between the AGB and the post-AGB phase. Evolved objects as post-AGB and pre-PN have larger infrared excesses than AGB envelopes.

- the AGB stars and the inner parts of the mid-IR envelopes are orders of magnitude brighter than the extended dust envelopes; a large S/N ratio is thus needed to separate the faint envelope emission from the stellar one.

On the other hand, many AGB sources are close to the solar system ($\lesssim$500 pc) and bright enough at 10 μm ($\gtrsim$500 Jy) that the conditions to attempt their imaging are satisfied by current mid-IR cameras and telescopes.

The scientific importance of such observations is to provide observational constraints on the physics of mass loss in late stages of stellar evolution. The questions raised in chapter 4, about a connection between stellar pulsations and dust production, can be directly tested by imaging the spatial structure of nearby AGB envelopes.

Growing evidences indicate an important role of non uniform density distributions in the dust forming regions of AGB stars (Le Bertre & Winters, 1998; Fleisher et al., 1992). Recent observations at different wavelengths support the idea that these inhomogeneities can propagate in the circumstellar envelope, giving rise to strong deviations from spherical symmetry. Clumpy structures in the dust forming regions of the C-rich AGB star IRC+10216 were found by near-IR masking and speckle interferometry at Keck and SAO telescopes (Monnier et al., 1997; Weigelt et al., 1998). A sequence of detached dust shells were also found around this source by deep optical imaging (Mauron & Huggins, 1999), suggesting a complex mass loss history similar to the one that characterized the more evolved post-AGB "Egg Nebula" (Sahai et al., 1998) or the O-rich Mira R Hya (Hashimoto et al., 1998). All these observations suggest that the asymmetry observed in many PN already starts during the AGB, where it shapes the evolution of the circumstellar envelope towards the Planetary Nebula phase.

This section describes an observational effort aimed to demonstrate the feasibility of AGB circumstellar envelopes mid-IR imaging with a mid-size infrared telescope. A technique developed for imaging objects having angular sizes comparable to the instrumental PSF is also described, and the results of the observations are presented.

5.4.1 The camera MIRAC3 at IRTF

MIRAC3 (Hoffmann et al., 1998) is a Mid-InfraRed Array camera which utilizes a Boeing HF16 128×128 Si:As hybrid BIB array. Reflective optics in the camera liquid-helium cryostat yield achromatic diffraction-limited imaging at a nominal scale on IRTF of 0.35"/pix, with zoom capability from 0.35 to 0.17"/pix. A PC with a Digital Signal Processor (DSP) card controls the telescope secondary chopper and data acquisition, storage, processing and display, and initiates telescope nod and offset motions via ethernet or RS232. From the full set of filters available for the camera, we have made use of the 10% filters centered at 8.8, 9.8, 11.7, 12.5 and 18.0 μm. The target sources were typically observed in all four chop-nod beams.

The observations were made with MIRAC3 at the 3 m aperture NASA InfraRed Telescope Facility (IRTF) on top of Mauna Kea (Hawaii). The project was awarded a total of 9 nights in November 1998 (3 full nights lost because of bad weather), June 1999 and September 1999.

Typical sensitivities expected at IRTF are 26 Jy arcsec^{-2} at 11.7 μm and 170 mJy arcsec^{-2} at 18.0 μm, all chop-nod, one minute total observing time.

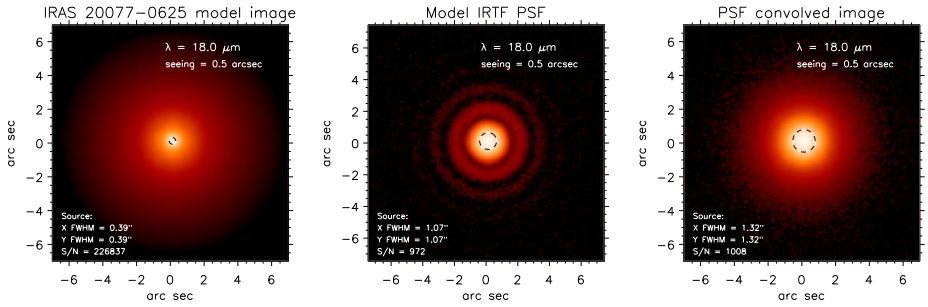

FIG. 5.11.— Simulated images of AGB circumstellar envelopes for the MIRAC3 camera at IRTF. Left panel shows the source model. The synthetic PSF with 0.5" and added noise is at the center. Final image (with $S/N \sim 1000$) is on the right.

5.4.2 Characterizing a sample of extended AGB sources

A critical part of our project was the selection of the sources to be imaged. To maximize the chances of extended emission detection one has to search for close-by objects having large optical depths, providing high infrared excess and extinction of the stellar radiation.

To find the best candidate meeting these criteria, we have modeled all AGB sources with $S/N \gtrsim 10$ in the IRAS LRS catalog by using the model grids described in chapter 3 for oxidic and carbonaceous dust. The sources were then selected with the following procedure:

1. the radial brightness distribution at 10 and 18 μm was computed for each envelope by fitting its IRAS Low Resolution Spectra;

2. a two dimensional image of each source was then derived from the intensity profile (figure 5.11, left panel);

3. the IRTF ideal diffraction limited PSF was simulated at 10 and 20 μm 10% passband filters. A more realistic PSF was then obtained by coadding many randomly displaced diffraction patterns in order to simulate a seeing of 0.5" (figure 5.11, center);

4. each source image was convolved with the PSF, and then resampled into the MIRAC3 final image array grid (0.32"/5, assuming a super-sampling of 5×5 pixels in the image reduction processing as described in section 5.2.3);

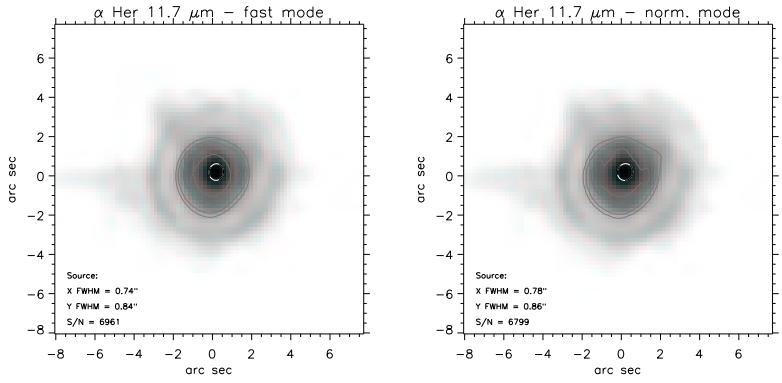

FIG. 5.12.— The reference star α Her at 11.7 μm. The image on the left was obtained using MIRAC3 fast mode, coadding about 1,600 single exposures of 0.17 sec (272 sec total); on the right is the coadding of 80 exposures of 10 sec each (800 sec total).

5. gaussian noise was added to all final images, to produce a peak S/N of ∼1,000, as expected for the real observations (figure 5.11, right);

6. the PSF was finally subtracted from the simulated images to map the excess of the source intensity with respect to the emission of a point source: detection of extended emission is expected only when this excess is above the noise level of the detector.

Note in figure 5.11 the well visible 2–3 diffraction rings in the model PSF, separated by dark annulus in which the flux of the PSF is below the noise. Note also in the right panel how the extended sources do not show the same pattern, having a much smoother profile. This is the main difference between extended sources of small angular size and point sources, and should be expected in the images of the observed AGB envelopes.

A criteria for selecting the sources showing a detectable extended emission is given by the ratio between the total excess flux and the normalized PSF in a standard 5" aperture:

$$ex = \frac{\sum_{ij} [\mathrm{image}(x_i, y_j) - \mathrm{PSF}(x_i, y_j)]}{\sum_{ij} \mathrm{PSF}(x_i, y_j)} \tag{5.13}$$

The best sources showing a detectable excess emission above the instrumental PSF in a minimum area of 6–8 arcsec in diameter were then selected for observations.

5.4.3 Observing technique

The circumstellar dust emission predicted by our models is typically characterized by a compact component, only partially resolved as an enlarged (in terms of the FWHM) PSF, plus a faint "halo" that can be separated by the "wings" of the PSF only when the S/N is of the order of ∼1,000 or larger. For a positive detection of these two components is necessary to maximize the achievable angular resolution and sensitivity. To meet these requirements, we used a rather short integration time (10 seconds), in order to reduce the effects of the atmospheric seeing. Hundreds of single chop-nod images were then taken, recentered and coadded as explained in section 5.2.3. This technique is possible in the case of AGB circumstellar envelopes because of the presence of a bright central source, which allows a precise recentering of the individual frames.

Another advantage of having many short integration time frames instead of a single long exposure, is a better spatial sampling of the images. To have even superior sampling we applied a dithering pattern to each beam position, by moving the sources in 5 offset positions on the detector array grid. An example of the full chop-nod sequence with dithering can be seen in the cumulative raw image shown in figure 5.5.

The optimal resolution can in principle be obtained by further reducing the single frame integration time. At mid-IR wavelengths, a frame time of the order to 0.1–0.2 sec is comparable to the timescale of the atmospheric convective cells turbulence. Setting this parameter to such a short time does in fact allow to "freeze" the atmospheric seeing, providing nearly perfect diffraction limited images. Again, this technique can be used only in case of very bright sources, for which a 0.1 sec integration time gives enough S/N for a precise recentering. A very fast data acquisition electronic system is also required, in order to be able to collect images at a rate of nearly 10 Hertz. This is possible in the case of MIRAC3, thanks to the special "fast mode" which saves the large number of observed frames in a packed format, with only a small increase of wait time for readout, A/D conversion and save to disk operations.

The "fast mode" technique produced an effective increase in the spatial resolution of the sources for which it was tested. An example is shown in figure 5.12, where the standard star β Her is shown, imaged with a frame time of 0.17 (left panel) and 10 seconds (right). The fast mode image is the coadd (with drizzling) of about 1,600 single exposures for a 272 sec total, while the normal integration was made with only 80 individual exposures (without drizzling), for a total time of 800 sec. Note the smaller FWHM

of the fast mode image, and its higher S/N, despite the shorter integration time.

Our tests showed that the fast mode technique can enhance the spatial resolution at 10 μm by about 5%. This can be crucial when the sources to be observed are of comparable size with the PSF. The gain in the spatial resolution is however only effective when the telescope PSF remains stable between the observation of the source and the reference star. As shown in the next section, this is not always the case for the IRTF, whose mirror does not possess the necessary rigidity to guarantee a completely stable PSF while pointing at different coordinates in the sky. In this case the induced PSF deformations are larger than the loss of spatial resolution due to the seeing reduction between the 0.1 and 10 seconds frame time integration. This technique is however recommended at telescopes equipped with active optics systems, which can take full advantage of the increased angular resolution.

5.4.4 Observed sources

The list of the observed sources is shown in table 5.5. It consists of 26 objects, of which 20 are O-rich, 6 C-rich, 1 S-star and 1 pre-PN. The 10 μm fluxes goes from 100 to 5000 Jy, with an average of 500 Jy, which required a total integration time of 10–15 min for source, and for filter. The standard stars α Boo, α Her, α Tau, β Peg, β And and γ Dra were observed for flux and PSF calibration.

The images were collected in the 10% passband filters at 8.5, 9.8, 11.7, 12.5 and 18.0 μm filters. A preference was given to the 18.0 μm filter, which our models show as having the best chance of detecting extended emissions above the PSF. This result of our simulations is not surprising, since the radiation emitted at 18 μm is originated in a colder region of the envelopes, which is thus more external. Since the temperature gradient in the envelopes goes as $T_d \sim r^{-0.3}$ (see equation 2.38), the region where a 20 μm photon is emitted is 8 times farther from the central star than the 10 μm photosphere. The 20 μm diffraction limited PSF is instead only 2 times larger than the 10 μm one (equation 5.7), and less subjected to the atmospheric seeing. It is thus easier to detect the extended emission of AGB circumstellar envelopes when the wavelength is longer. The only limit in this approach is in the lower brightness of 18 μm emissions. This is not a problem for our selected bright sources though it could be, for the standards which are in general less luminous than the AGB sources. The 11.7 μm filter was also favored, since it is in the middle of the 10 μm window, where the atmosphere is more transparent and the detector more sensitive.

Table 5.5 List of MIRAC3 sources

Source	Type	IRAS name	F12 [Jy]	F25 [Jy]	Var. type
WX Psc	O-rich	01037+1219	1160	968	-
V370 And	O-rich	01556+4511	499	291	-
o Cet	O-rich	02168−0312	4880	2260	M
V656 Cas	O-rich	02316+6455	481	314	M
IRC+50096	C-rich	03229+4721	535	199	-
IK Tau	O-rich	03507+1115	4630	2380	M
TX Cam	O-rich	04566+5606	1640	635	M
V Hya	C-rich	10491−2059	1110	460	-
V CVn	O-rich	13172+4547	132	64	SR
W Hya	O-rich	13462−2807	4200	1190	SR
OV Ser	O-rich	15223−0203	101	67	-
X Her	O-rich	16011+4722	484	241	SR
IRC+20370	C-rich	18397+1738	534	239	M
IRC+10401	C-rich	19008+0726	454	182	M
W Aql	S-star	19126−0708	1575	670	M
CH Cyg	O-rich	19232+5008	565	191	SR
V1302 Aql	pre-PN	19244+1115	1350	2310	-
GY Aql	O-rich	19474−0744	460	271	SR
BI Cyg	O-rich	20194+3646	335	245	-
V Cyg	C-rich	20396+4757	665	234	M
T Cep	O-rich	21088+6817	753	267	M
EP Aqr	O-rich	21439−0226	637	321	-
IRC+40540	C-rich	23320+4316	959	469	-
R Aqr	O-rich	23412−1533	1580	543	M
TX Psc	C-rich	23438+0312	163	40	-
R Cas	O-rich	23558+5158	1340	555	M

To minimize the spatial dependence of the PSF from the atmospheric conditions and telescope orientation we have always observed the closest standard before and after each source, in each filter.

The data reduction and photometric calibration was performed as described in section 5.2, using the IDL package we wrote and optimized for our

Table 5.6 Photometry of MIRAC3 sources

Source	$F_{8.5}$ [Jy]	$F_{9.8}$ [Jy]	$F_{11.7}$ [Jy]	$F_{12.5}$ [Jy]	$F_{18.0}$ [Jy]	epoch
WX Psc	-	-	1580	1370	2380	Sep 99
V370 And	-	-	403	393	-	Sep 99
o Cet	-	2710	2170	-	2020	Sep 99
V656 Cas	-	-	214	-	231	Sep 99
IRC+50096	-	-	500	-	281	Sep 99
IK Tau	-	-	2080	-	2060	Sep 99
TX Cam	-	-	917	762	976	Sep 99
V Hya	-	-	1120	-	628	Jun 99
V CVn	105	175	109	88	115	Jun 99
W Hya	-	2000	2940	2770	1780	Jun 99
	-	-	2850	-	-	Jun 99
OV Ser	78	101	87	77	81	Jun 99
X Her	490	-	503	451	408	Jun 99
IRC+20370	-	-	994	781	440	Jun 99
IRC+10401	-	-	449	396	237	Jun 99
W Aql	-	-	983	885	725	Sep 99
CH Cyg	-	-	639	483	558	Jun 99
V1302 Aql	788	-	1380	-	2570	Jun 99
GY Aql	-	-	505	198	432	Sep 99
BI Cyg	-	-	280	201	332	Sep 99
V Cyg	-	-	20	19	312	Jun 99
T Cep	-	-	554	-	377	Sep 99
EP Aqr	-	-	499	-	481	Sep 99
IRC+40540	-	810	791	707	595	Sep 99
R Aqr	-	1170	-	-	699	Sep 99
TX Psc	-	-	105	-	54	Sep 99
R Cas	-	2200	1640	1430	1310	Sep 99

observing technique. The fluxes of the standard stars come from Hoffmann & Hora (1999).

The photometry of the sources is listed in table 5.6. Relatively stable conditions of the Mauna Kea sky on the timescale of each source-standard pair observations were met in most of our June and September 1999 runs. In these conditions the photometric accuracy computed for the flux density in table 5.6 are of ∼5% for the 8.5, 9.8, 11.7 and 12.5 μm filters, and ∼8% at 18 μm.

The measured photometry is mostly in accordance with the IRAS fluxes at 10 and 20 μm, taking into account the different filter profiles and effective wavelengths, and the long period variability of all the sources.

Table 5.7 FWHM of MIRAC3 sources, references and deconvolutions.

Source	λ	FWHM Source		FWHM Reference		FWHM Max Entropy		FWHM Max Likelihood		excess
	[μm]	X ["]	Y ["]	X ["]	Y ["]	X ["]	Y ["]	X ["]	Y ["]	
WX Psc	11.7	0.77	0.86	0.75	0.83	0.22	0.29	0.23	0.29	0.0%
	18.0	1.24	1.13	1.08	1.11	0.54	0.43	0.52	0.43	**23.4**%
V370 And	11.7	0.78	0.84	0.75	0.83	0.24	0.25	0.25	0.27	3.1%
	12.5	0.87	0.84	0.85	0.83	0.26	0.27	0.26	0.27	4.2%
o Cet	9.8	1.04	0.92	0.85	0.95	0.38	0.36	0.37	0.38	18.7%
	11.7	0.93	1.03	0.85	0.95	0.35	0.35	0.35	0.38	15.5%
	18.0	1.35	1.40	1.12	1.08	0.68	0.71	0.68	0.71	**63.0%**
V656 Cas	11.7	0.90	1.01	0.83	0.90	0.30	0.35	0.30	0.34	**30.7%**
	18.0	1.15	1.23	1.10	1.03	0.72	0.66	0.45	0.72	**24.7**%
IRC+50096	11.7	0.87	0.90	0.88	0.78	0.28	0.39	0.27	0.39	8.3%
	18.0	1.18	1.28	1.12	1.08	0.53	0.57	0.58	0.70	**33.9%**
IK Tau	11.7	0.81	0.83	0.88	0.78	0.21	0.28	0.22	0.27	0.0%
	18.0	1.13	1.15	1.12	1.08	0.70	0.70	0.65	0.66	11.9%
TX Cam	11.7	0.93	0.91	0.80	0.78	0.30	0.41	0.32	0.41	**31.7%**
	12.5	0.96	0.93	0.85	0.83	0.31	0.37	0.31	0.38	**27.9%**
	18.0	1.37	1.34	1.14	1.06	0.49	0.68	0.50	0.71	**71.5%**
V Hya	11.7	0.82	0.97	0.81	0.95	0.25	0.32	0.25	0.33	4.9%
	18.0	1.15	1.35	1.07	1.23	0.53	0.80	0.48	0.63	**21.4%**
V CVn	8.8	0.73	0.90	0.76	0.87	0.24	0.31	0.23	0.31	4.8%
	9.8	0.77	0.81	1.25	0.92	0.26	0.28	0.25	0.25	0.0%
	11.7	0.87	0.83	0.82	0.99	0.29	0.23	0.29	0.24	0.0%
	12.5	0.85	0.87	0.85	1.06	0.27	0.22	0.28	0.23	0.0%
	18.0	1.09	1.13	1.05	1.14	0.50	0.56	0.38	0.36	19.7%
W Hya	9.8	0.82	0.99	0.79	0.84	0.28	0.41	0.28	0.41	**26.7%**
	11.7	0.88	1.04	1.12	1.24	0.25	0.37	0.27	0.36	**35.6%**
	11.7	0.86	0.98	0.87	0.83	0.27	0.40	0.28	0.40	18.8%
	12.5	0.98	1.06	0.85	0.89	0.35	0.45	0.36	0.46	**44.7%**
	18.0	1.19	1.43	1.10	1.17	0.48	0.80	0.48	0.80	**45.6%**
OV Ser	8.8	0.81	0.77	0.80	0.83	0.23	0.25	0.23	0.25	0.0%
	9.8	0.83	0.92	1.25	0.92	0.27	0.38	0.26	0.33	0.0%
	11.7	0.82	0.95	1.07	0.92	0.21	0.32	0.22	0.32	0.0%
	18.0	1.20	1.33	1.24	1.21	0.47	0.86	0.46	0.85	4.4%

Table 5.7: continue.

	λ	FWHM Source		FWHM Reference		FWHM Max Entropy		FWHM Max Likelihood		excess
	[μm]	X ["]	Y ["]	X ["]	Y ["]	X ["]	Y ["]	X ["]	Y ["]	
X Her	8.8	0.78	0.80	0.73	0.83	0.27	0.23	0.27	0.23	0.1%
	11.7	0.84	0.89	0.83	0.91	0.28	0.25	0.27	0.28	0.0%
	12.5	0.85	0.89	0.92	0.87	0.27	0.25	0.27	0.25	0.0%
	18.0	1.18	1.18	1.07	1.19	0.65	0.52	0.52	0.41	10.5%
IRC+20370	11.7	0.85	1.07	0.80	0.91	0.28	0.46	0.29	0.46	17.1%
	12.5	0.88	0.94	0.86	0.92	0.27	0.29	0.28	0.30	0.0%
	18.0	1.22	1.33	1.10	1.19	0.43	0.50	0.45	0.52	**22.3%**
IRC+10401	11.7	0.83	0.92	0.80	0.91	0.25	0.29	0.26	0.29	5.3%
	12.5	0.84	0.91	0.86	0.92	0.22	0.27	0.24	0.27	0.0%
	18.0	1.15	1.28	1.10	1.19	0.33	0.48	0.37	0.46	11.6%
W Aql	11.7	0.91	0.84	0.86	0.88	0.26	0.33	0.26	0.33	0.0%
	12.5	0.85	0.91	0.87	0.87	0.29	0.34	0.29	0.32	2.48%
	18.0	1.20	1.123	1.08	1.11	0.52	0.64	0.47	0.57	**27.1%**
CH Cyg	11.7	0.87	0.84	0.79	0.84	0.31	0.29	0.26	0.33	4.3%
	12.5	0.90	0.87	0.87	0.85	0.33	0.36	0.31	0.32	0.1%
V1302 Aql	8.8	0.72	0.80	0.61	0.71	0.32	0.30	0.32	0.30	**27.5%**
	11.7	0.88	0.94	0.74	0.84	0.35	0.35	0.35	0.35	**28.3%**
	18.0	1.43	1.50	1.20	1.09	0.65	0.69	0.66	0.69	**49.5%**
GY Aql	11.7	0.85	0.85	0.88	0.82	0.26	0.30	0.26	0.30	0.0%
	12.5	0.84	0.89	0.91	0.84	0.29	0.29	0.27	0.28	0.9%
	18.0	1.20	1.13	1.10	1.03	0.62	0.66	0.50	0.63	19.3%
BI Cyg	11.7	0.92	0.86	0.86	0.88	0.32	0.29	0.31	0.28	2.3%
	12.5	0.87	0.92	0.91	0.84	0.28	0.31	0.27	0.32	3.2%
	18.0	1.21	1.27	1.06	1.1	0.59	0.57	0.54	0.50	**32.8%**
V Cyg	11.7	1.16	1.13	0.77	0.85	0.84	0.87	0.84	0.80	**101.5%**
	12.5	1.14	1.07	0.86	0.84	0.86	0.90	0.80	0.74	**69.3%**
	18.0	1.17	1.17	1.14	1.07	0.61	0.57	0.48	0.46	17.1%
T Cep	11.7	0.83	0.90	0.84	0.76	0.27	0.46	0.27	0.43	16.4%
	18.0	1.10	1.26	1.01	1.06	0.59	0.87	0.53	0.83	**37.6%**
EP Aqr	11.7	0.83	0.89	0.84	0.79	0.27	0.35	0.27	0.35	7.2%
	18.0	1.18	1.18	1.10	1.03	0.54	0.75	0.52	0.65	**22.8%**
IRC+40540	9.8	0.77	0.89	0.90	0.75	0.23	0.32	0.24	0.32	3.6%
	11.7	0.86	0.90	0.89	0.80	0.26	0.32	0.26	0.32	6.8%
	12.5	1.00	1.10	0.85	0.87	0.41	0.55	0.41	0.57	**48.9%**
	18.0	1.27	1.45	1.22	1.12	0.52	0.70	0.51	0.71	**42.3%**

Table 5.7: continue.

	λ	FWHM Source		FWHM Reference		FWHM Max Entropy		FWHM Max Likelihood		excess
	[μm]	X ["]	Y ["]	X ["]	Y ["]	X ["]	Y ["]	X ["]	Y ["]	
R Aqr	9.8	0.89	1.00	0.85	0.95	0.31	0.35	0.31	0.35	8.7%
	18.0	1.27	1.29	1.14	1.06	0.54	0.68	-	-	**34.7%**
TX Psc	11.7	0.85	0.81	0.83	0.90	0.28	0.23	0.28	0.23	0.0%
	18.0	1.12	1.20	1.14	1.06	0.44	0.51	0.42	0.38	14.8%
R Cas	9.8	0.88	0.86	0.90	0.75	0.27	0.32	0.27	0.33	13.0%
	11.7	0.89	0.90	0.89	0.80	0.26	0.33	0.27	0.33	15.2%
	12.5	1.00	1.13	0.85	0.87	0.38	0.55	0.38	0.56	**55.9%**
	18.0	1.32	1.52	1.22	1.12	0.56	0.78	0.57	0.79	**67.6%**

5.4.5 Discussion

Table 5.7 shows the extension of all observed sources, measured with the same criteria used for the source selection, which applies equation 5.13 to each source - reference pair renormalized to their peak value:

$$\text{source}' = \frac{\text{source}}{\text{MAX[source]}} \quad , \quad \text{reference}' = \frac{\text{reference}}{\text{MAX[reference]}} \tag{5.14}$$

Boldface numbers indicate source excess emission above 20% of the PSF total flux. Negative values have been set to zero (this is the case when the reference is more extended to the source, generally due to bad focusing of the telescope).

From a total of 75 observations, 28 show more than 20% of extended emission above the PSF, corresponding to 17 sources extended at least at one wavelength, on a sample of 26. In general, sources extended in one filter tend to show measurable infrared excess also in the other wavelengths, but in most cases the larger excess is measured at 20 μm. This result was fully expected, as explained in the previous section.

For each source and reference star, table 5.7 reports the FWHM in the X and Y direction, where X is oriented in R.A. and Y in declination. With only a few exceptions, all sources have a larger FWHM than the corresponding standards, with a difference that is in some cases larger than 1 MIRAC pixel (0.33" for June observations, 0.34" in September).

The maximum entropy and maximum likelihood (Lucy method) deconvolutions have been computed for all source and reference pair. The FWHM

of the deconvolved images are also listed in table 5.7. Due to the limitations in the deconvolution algorithms, the given value should be used with caution, and considered only as an upper limit for the source "sizes". Tests made by convolving pairs of reference stars show that in general a residual image is left by both deconvolution processes, that can be as big as 1 MIRAC pixel.

5.4.6 Images of individual sources

The next pages show images of a few extended sources from our observed sample. Each figure plots the image of the source at a certain wavelength, the reference star in the same filter, the infrared excess image, obtained by subtracting the renormalized reference from the source, and the maximum entropy deconvolution. The orientation of the images is N up and W right. The source and reference image also show the contours at 0.01, 0.02, 0.05, 0.1, 0.2 of the maximum. The half maximum ellipse (contour at 0.5 of the maximum) is also plotted (dashed circle).

Most of the images are at 18 μm, where the extension is more evident, and the PSF is less dependent from the seeing. In some cases the images at shorter wavelengths are also shown for comparison.

Almost all sources show departures from spherical symmetry on angular size much larger than the telescope resolution. These deviation from sphericity however are generally present at a low brightness level, and can be due to the instability of the IRTF PSF with respect to the telescope orientation. We have indeed verified that the same standard observed in different positions on the sky can generate asymmetric features in the PSF. For this reason we cannot claim in some cases a specific symmetry of the observed sources, on the basis of our images alone. Active optics telescopes, providing a controlled shape of the primary mirror, can in principle overcome this difficulty, and allow the analysis of geometry of AGB circumstellar envelopes in greater detail.

Many deconvolved images appear to have ring like structures, analogous to detached shells. When the observed rings appear at the same position of the PSF diffraction minima, they are artifacts of the deconvolution process, which tends to concentrate the flux where the S/N ratio is higher. In the case of our AGB envelopes, which have a smoother radial profile than the instrumental PSF (see e.g. figure 5.11) the maximum signal of the excess emission is precisely where the PSF disappears, that is in the minima of its diffraction pattern. The presence of the rings is a confirmation of the spatial extension of the source, and can give an idea of the real size of the

envelopes. However, they cannot be considered as detached shells without independent observations.

The best case which suggests the presence of a detached envelope is the deconvolved image of W Hya (figure 5.23) at 18 μm. The high S/N of both source and reference, and the net separation of the observed ring from the central source, is an indication that the shell can be physically disconnected from the star, by a phase of less intense mass loss. The shell is elongated in the N-S direction, and has a very different shape than the second diffraction ring of the PSF. The same structure is observed in the deconvolved images at other wavelengths. These are strong evidences that the detached appearence of the shell is not a spurious result of the deconvolution process.

Along with the detached shell, the source shows a second, compact envelope around the AGB star. This compact source is also extended (according to the FWHM of the deconvolved image), and very elongated, also in the N-S direction.

If the 18 μm shell observed in our image is detached, its separation from the central star ($\sim$ 2.5 arcsec) would correspond to a distance of $\sim$ 280 A.U. from the star, given the parallax of the source measured by HIPPARCOS (8.73mas, Perriman et al. 1997). With an expansion velocity of 8.2 km s^{-1} (Loup et al., 1993), the timescale for the separation of the envelope would be $\sim$ 170 yr.

A detailed model of the source, fitting the observed radial brightness distribution, is in progress, and should give more information on the spatial structure of the source. A follow-up observation with a larger aperture telescope is also programmed.

Since W Hya is an O-rich SR variable, the presence of a detached shell, if confirmed, would be in nice agreement with the predictions made in chapter 4. Note, as a comparison, the symmetric shape of the deconvolved image of the Mira prototype *o* Cet (figure 5.22), which suggests an extended spherical envelope attached to the source. Even though shorther wavelength observations indicate asymmetries of *o* Cet photosphere (Karovska et al., 1997; Lopez et al., 1997), these deviations from spherical symmetry are not confirmed in our images.

Among the sources which show extension in our MIRAC3 data, there is also the O-rich AGB star WX Psc, which was already observed with the camera CAMIRAS (see section 5.3.4). An extended envelope is detected only at 18 μm, and does not show the asymmetry of figure 5.10 (the deconvolved image is symmetrical). The FWHM at 18 μm is elongated in the E-W direction, while the 11.7 μm FWHM is N-S elongated. This discrepancy is a suggestion that the asymmetries observed in CAMIRAS images may be

due to an incorrect shape of the PSF.

Among the other observed sources, the largest extensions are shown by IRC+20370 (6"×8", probably asymmetrical), TX Cam (with a 6"×7" asymmetric halo) and the post-AGB V1302 Aql which is strongly extended at all wavelengths. This last source was previously imaged with MIRAC at the IRTF (Meixner et al., 1999), and was found extended and elongated, with major axis at 45° (9.8 μm) and 63° (20.6 μm) counterclockwise N to E. Our deconvolved images, which are characterized by a better angular resolution provided by the "fast mode" and drizzling technique used for this source, confirm the observed asymmetry. The full size of the envelope, given by the deconvolved images, is 4"×3" at 11.7 μm and $\sim$ 5" at 18.0 μm.

5.4.7 Conclusions

Our observations have demonstrated that high resolution imaging of AGB circumstellar envelopes is feasible with current mid-IR cameras and telescopes. All observed sources, selected by modeling their mid-IR spectrum, have shown some degree of extension, which in two third of the cases is larger than 20%.

The observed sources are more extended at 20 μm, where the radiation is emitted by the external regions of their envelopes. Deconvolution techniques are applied to the images, and reduce the effects of seeing and diffraction. The sub-arcsec angular resolution provided by our deconvolved images, allows to infer the spatial distribution of dust around the central stars. Despite some limitations due to the unstable PSF of the IRTF telescope, our deconvolutions give strong constraints on the symmetry of the sources, and the eventual presence of detached shells. Previously observed images of our sources, when available, confirm the symmetry and extension suggested by our images.

A follow-up campaign with the larger MMT telescope (6m aperture), equipped with active optics able to increase the stability of the PSF, is programmed. The new observations will be carried on to confirm the results of our survey, and extend the sample to lower luminosities. Radiative transfer modeling of the extended sources, fitting at the same time the spectra and the radial brightness distribution of the envelopes, is also programmed. This combined analysis, compared to more traditional techniques, offers stronger constraints on the parameters of the envelopes, and is less dependent on the PSF instability. This will allow a much better understanding of the physics of mass loss in evolved stars, until now precluded by the absence of high resolution data at mid-IR wavelengths.

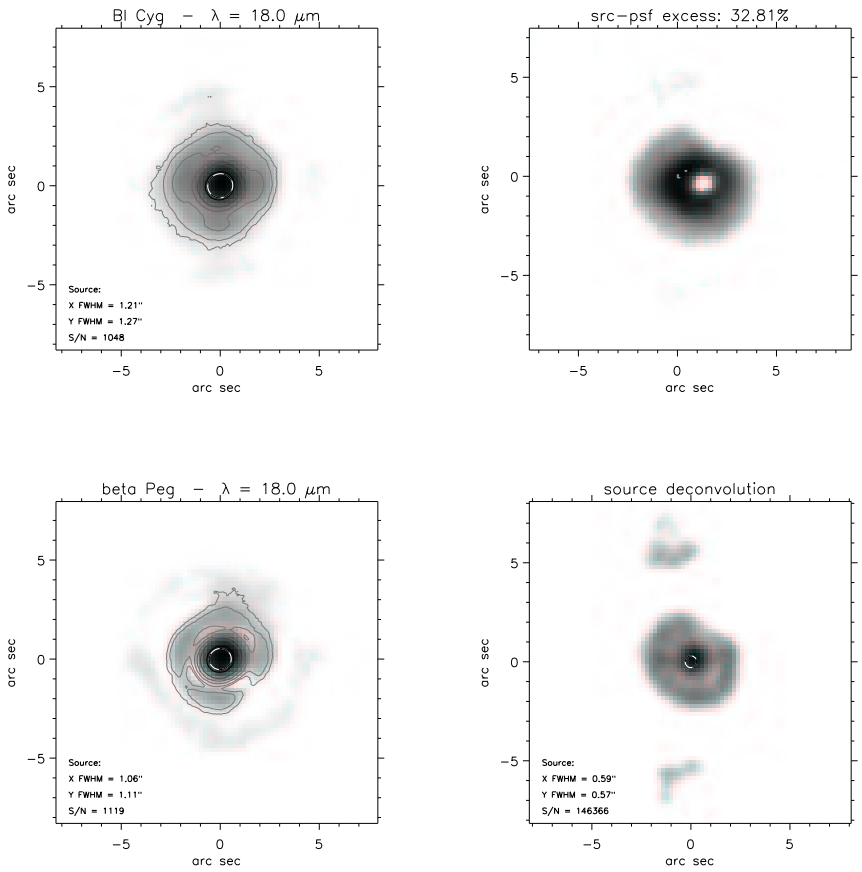

FIG. 5.13.— 18.0 μm image of the O-rich source BI Cyg, its reference star β Peg, the infrared excess image and their deconvolution. The source is only extended at 18.0 μm, while at shorter wavelength it is a point source. The two structures in the N-S direction visible in the deconvolved image, are probably an artifact of the deconvolution process. The source appears symmetric, with a total diameter of the circumstellar emission of 5".

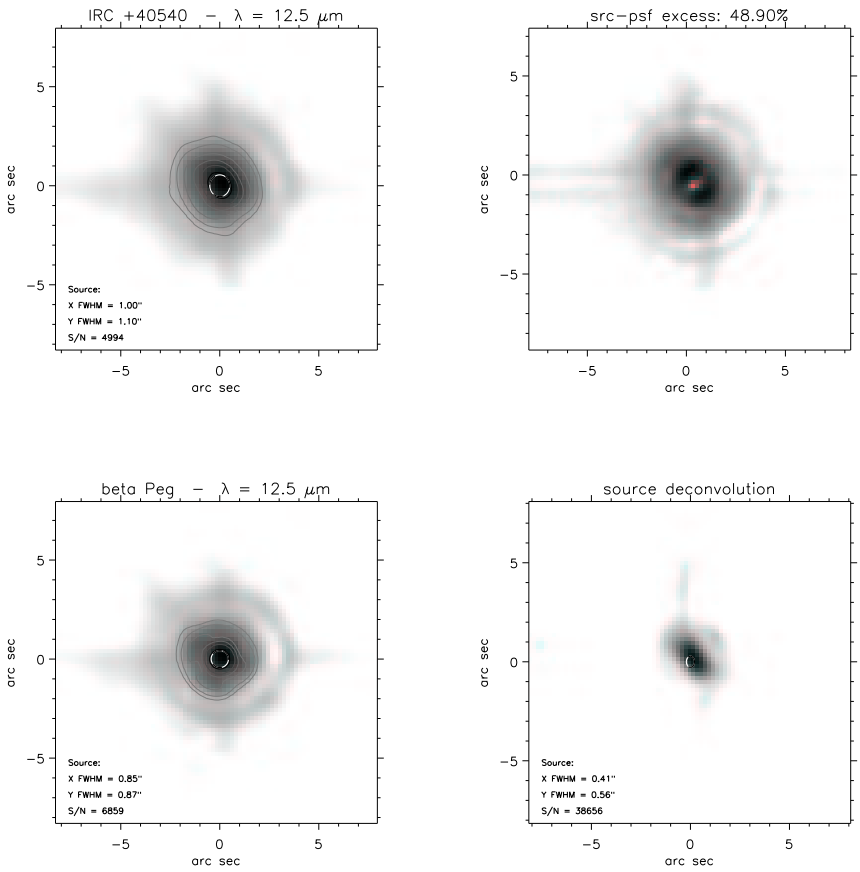

FIG. 5.14.— 12.5 μm image of the C-rich source IRC+40540, its reference star β Peg, the infrared excess image and their deconvolution. The source is also extended at 18.0 μm, but not at shorter wavelength. The source is elongated in the NE-SW direction, with size 3"×3".

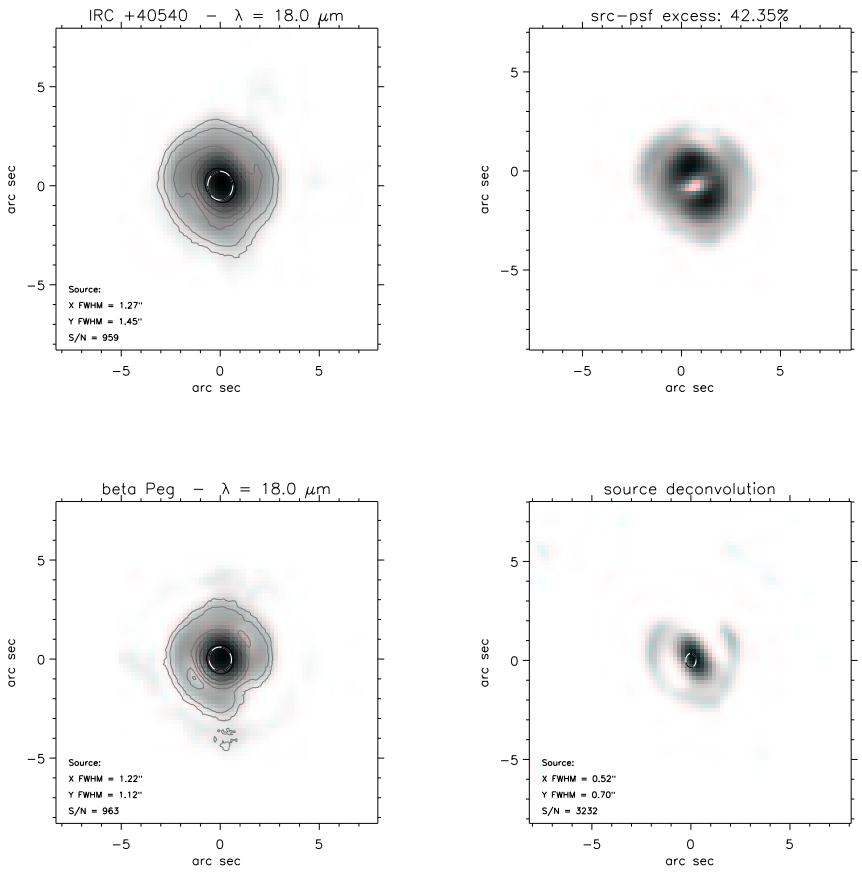

FIG. 5.15.— 18.0 μm image of the C-rich source IRC+40540, its reference star β Peg, the infrared excess image and their deconvolution. The image shows the same elongation seen at 12.5 μm, but the extended emission is here detected as far as the second diffraction ring (5").

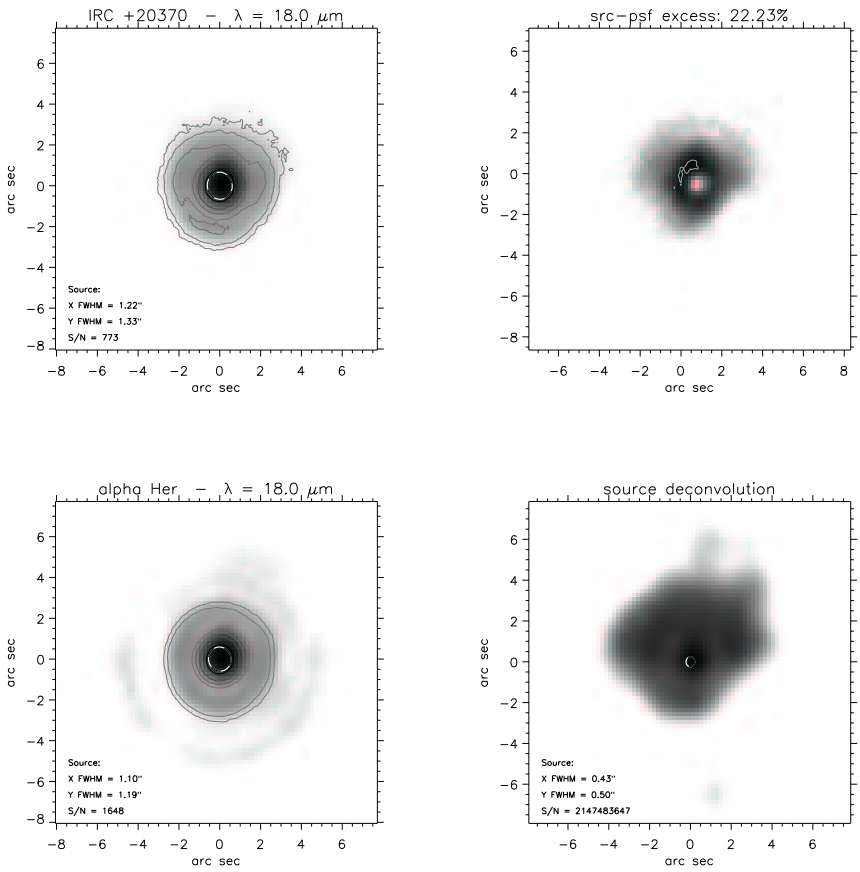

FIG. 5.16.— 18.0 μm image of the C-rich source IRC+20370, its reference star α Her, the infrared excess image and their deconvolution. The source appears also extended at 11.7 μm. The image in the 12.5 μm filter does not show extension because of low S/N ratio. The source shows a rectangular shape with high S/N, and an extension of 6"×8", mainly N of the central star.

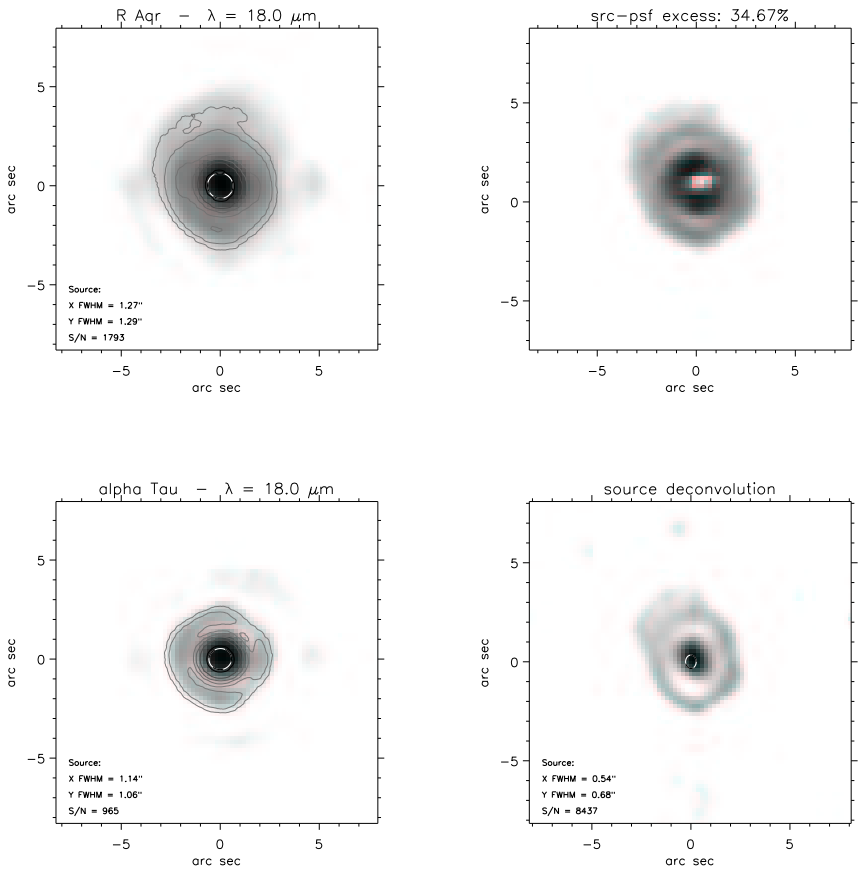

FIG. 5.17.— 18.0 μm image of the Mira O-rich source R Aqr, its reference star α Tau, the infrared excess image and their deconvolution. The source is not extended in MIRAC3 images at shorter wavelength. The extended emission is detected inside an area of 4"×6" around the central source. The oval shape is probably due to a deformed PSF, since the source was observed with airmass $\gtrsim$ 1.3.

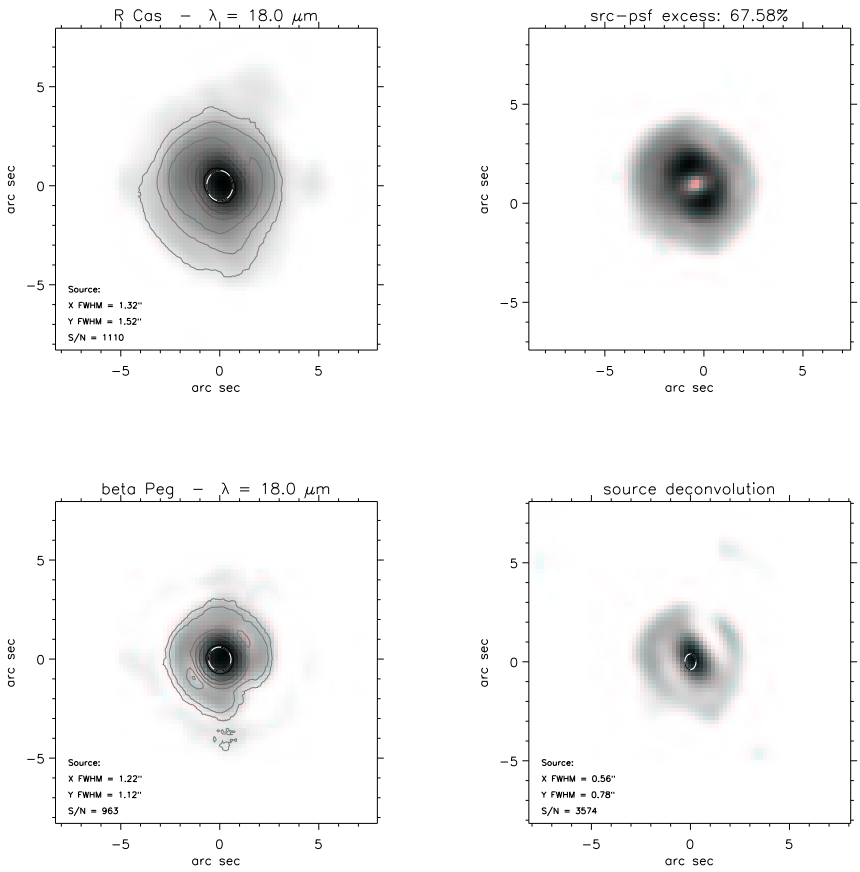

FIG. 5.18.— 18.0 μm image of the O-rich source R Cas, its reference star β Peg, the infrared excess image and their deconvolution. The source is extended at all wavelengths, showing an oval compact emission 0.55"$\times$0.76" plus an extended halo 6" in diameter.

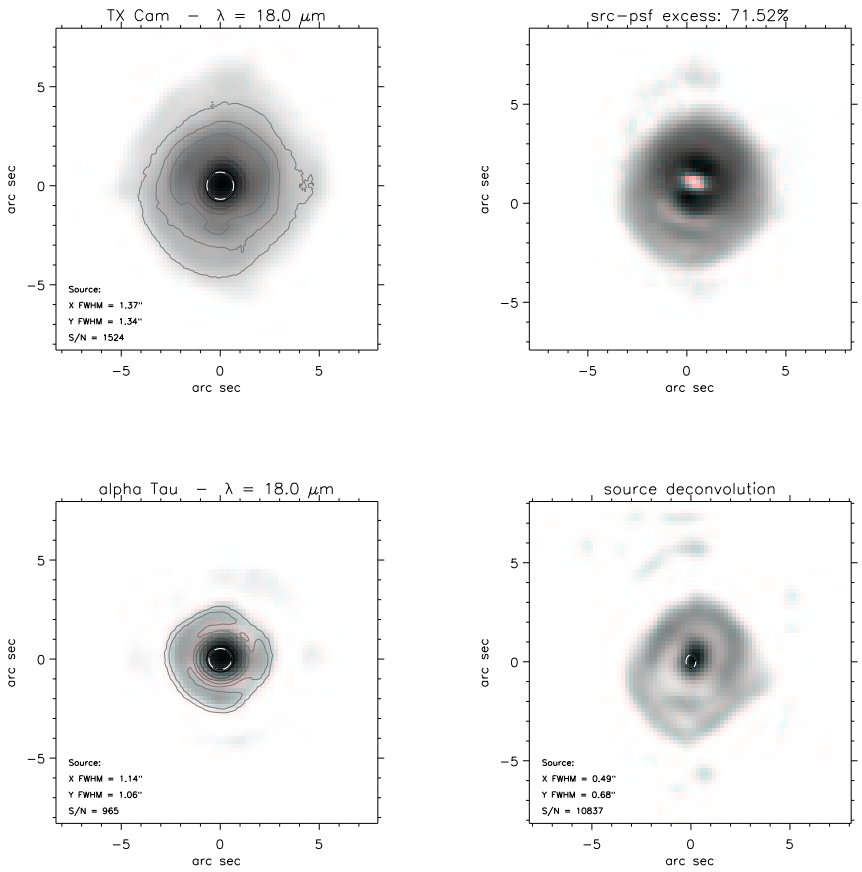

FIG. 5.19.— 18.0 μm image of the O-rich source TX Cam, its reference star α Tau, the infrared excess image and their deconvolution. The source is one of the more extended in our sample, with a 6"×7" halo. The source shows a larger and more diffuse IR excess S of the central star.

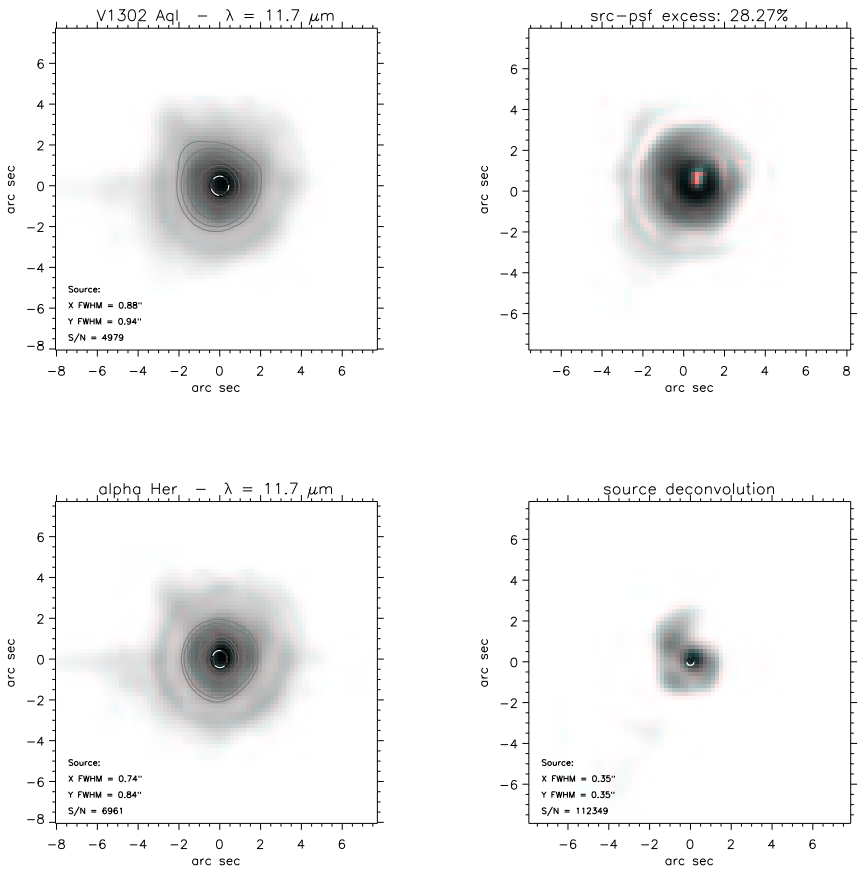

FIG. 5.20.— 11.7 μm image of the post-AGB source V1302 Aql, its reference star α Her, the infrared excess image and their deconvolution. The source is very extended in all filters, with a size of 4" even at short wavelength. The asymmetric structure of the source is confirmed by Meixner et al. (1999).

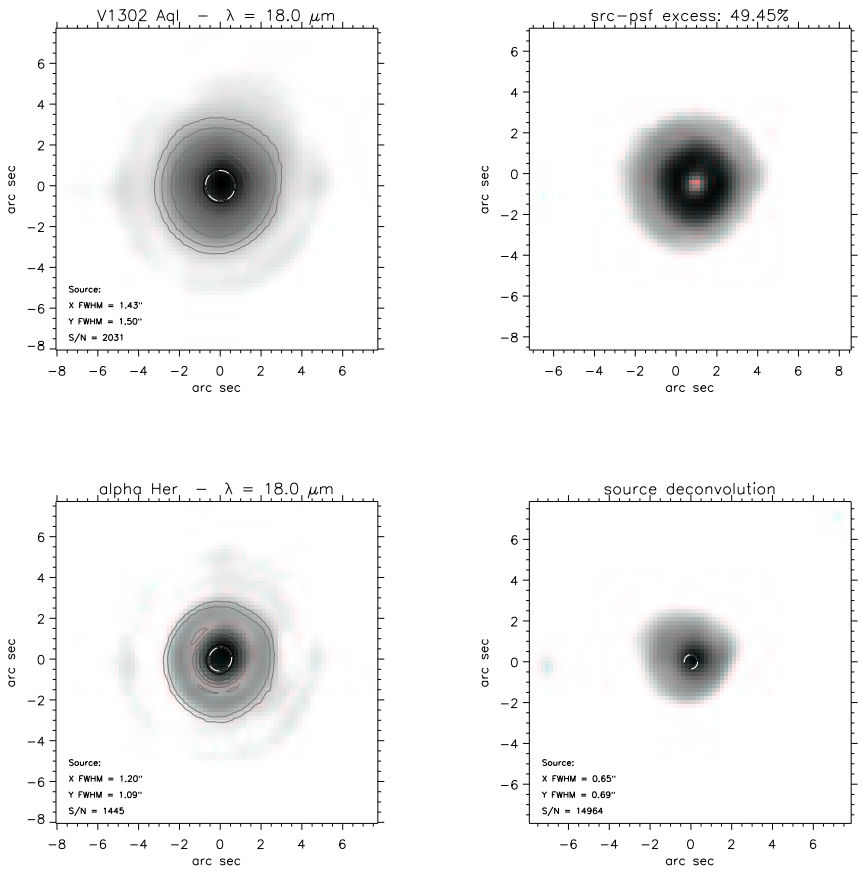

FIG. 5.21.— 18.0 μm image of the post-AGB source V1302 Aql, its reference star α Her, the infrared excess image and their deconvolution. The extension and symmetry of the source is confirmed, with a size of 5".

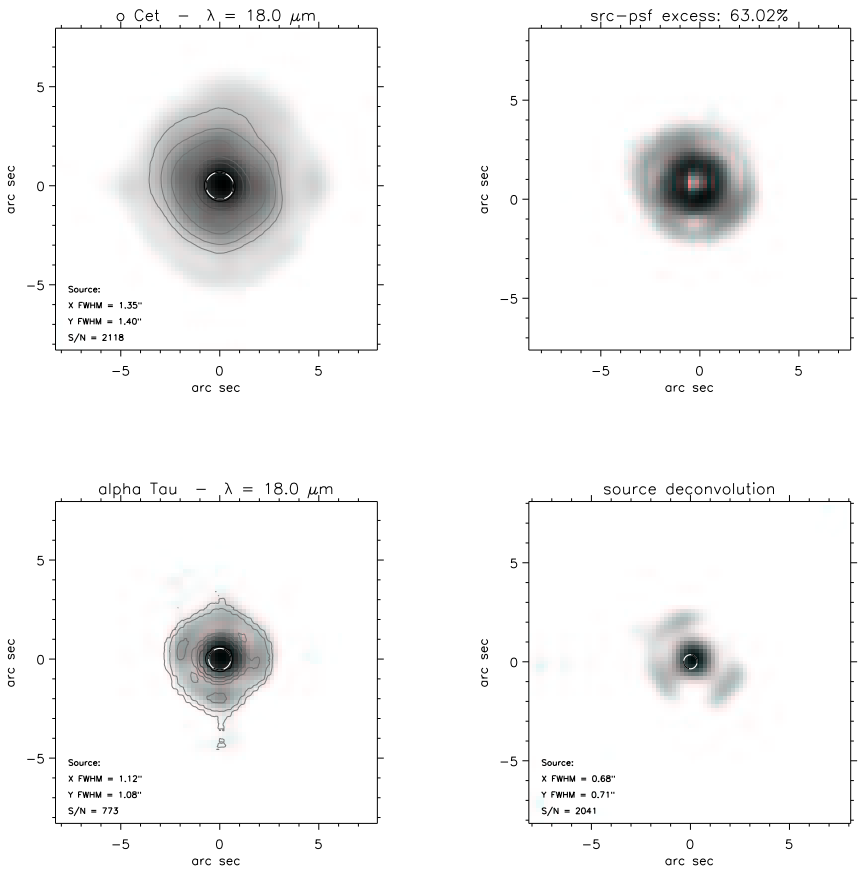

FIG. 5.22.— 18.0 μm image of the Mira prototype o Cet, its reference star α Tau, the infrared excess image and their deconvolution. The source is also extended at shorter wavelength with a size of 5" (after which the S/N is "killed" by the second diffraction ring). The clumpy structure is probably a consequence of a deformed PSF (observed with airmass $\gtrsim$ 1.25). The geometry of the envelope appears to be spherical at 18 μm, even though the source shows asymmetries and multiple shells at a much smaller spatial scale (Karovska et al., 1997; Lopez et al., 1997).

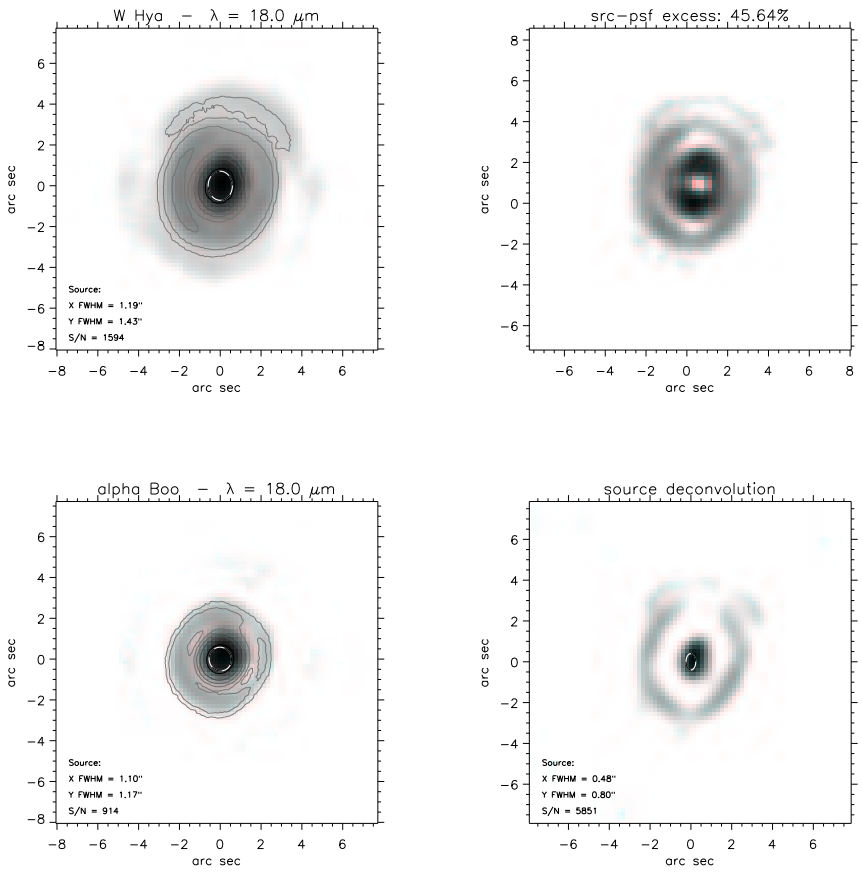

FIG. 5.23.— 18.0 μm image of the O-rich SR W Hya, its reference star α Boo, the infrared excess image and their deconvolution. The source appears extended at all wavelengths. Note the oval shape and the detached appearance of the deconvolved envelope.

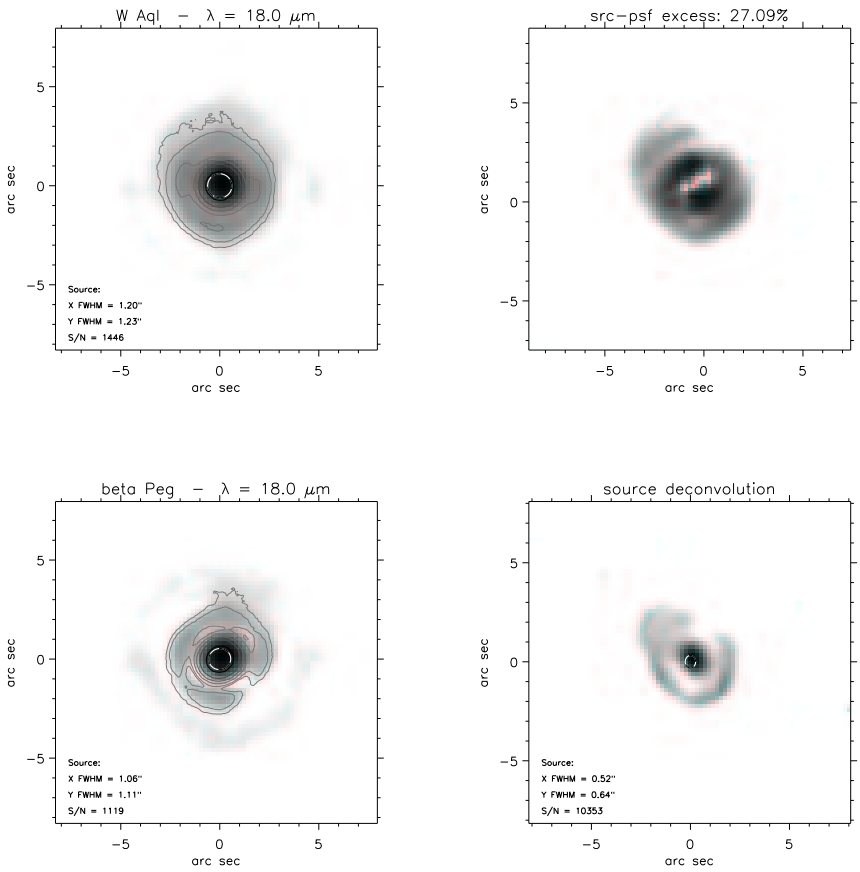

FIG. 5.24.— 18.0 μm image of the S-star W Aql, its reference star β Peg, the infrared excess image and their deconvolution. The source is extended only at this wavelength, up to the second diffraction ring of the image (after which the S/N is too low). The oval shape, as in the case of R Aql, is a consequence of the PSF.

5.5 AFGL 2591: detection of dust ejection in a massive YSO

During the MIRAC3 IRTF run, we have observed the bright Young Stellar Object (YSO) AFGL 2591. The images, taken at 11.7, 12.5 and 18.0 μm, revealed a knot of emission which may be evidence for a recent ejection event. This knot is roughly coincident with a previously seen near-IR reflection nebula and radio source, and lies within the known large-scale CO outflow. We also found a new faint NW source which may be an embedded low mass star. The results of the observations are described in this section, as published on Astrophysical Journal Letters (Marengo et al., 2000c).

5.5.1 Outflows in Young Stellar Objects

It is now generally agreed that most, if not all, stars produce energetic outflows during their formations (see Bachiller, 1996, for a review). Since the discovery of outflows almost 20 years ago (Snell et al., 1980), nearly 200 examples have been found, most of them associated with low luminosity YSO. Outflows can be studied using a variety of tracers including high velocity CO line emission (Bally & Lada, 1983), shock excited H_2 line emission (e.g. Lane, 1989) and optically visible Herbig-Haro (HH) jets (Reipurth 1989, 1999).

Even though all indications are that the flows emerge bipolarly from the stellar or circumstellar region, the physical processes giving rise to the outflows are not well understood. A primary wind originating at the star (e.g Shu et al., 1991) or at the accretion disk (e.g. Pudritz & Norman, 1983) is assumed to be responsible for the outward flow. A well collimated wind sweeps up the ambient molecular gas in its vicinity, forming two cavities in opposite directions from the star. The displaced molecular gas constitutes the CO outflows, and ionized "*knots*" of gas manifest themselves as HH objects. Outflows probably occur while the star is still accreting material, and may play a significant role in ejecting material of excess angular momentum.

The presence of "bullets" in the CO emission, and shocked "knots" visible in the optical and near-IR suggest that the mass ejection in YSO may occur intermittently, with an interval of $\sim 10^3$ yr between successive outbursts. The reasons for such modulation are not clear, but there are reasons to suspect a connection with variations in the accretion rate through a circumstellar disk (Hartmann & Kenyon, 1985). If this is true, it may be possible to probe the accretion history of protostars using detailed observations of their outflows (Reipurth, 1989).

One of the barriers to better understand the outflow process is the limited spatial resolution of CO observations. This is particularly true for YSOs which are embedded in dusty clouds responsible for large extinctions ($A_V \gg 10$).

These limitations can be overcome in the mid-IR, where sub-arcsec resolution can be provided by ground-based high resolution imaging, with the techniques explained in in section 5.2.

The observed source, AFGL 2591, was first recognized as an outflow by Bally & Lada (1983). The CO outflow is larger than 1' in extent, with the blue lobe extending west or southwest, and the red lobe in the northeast direction (Lada et al., 1984; Mitchell et al., 1992; Hasegawa & Mitchell, 1995). Optical and near-IR observations have revealed molecular hydrogen emission (40" east and west, Tamura & Yamashita 1992) and HH objects (10" and 20" west/southwest, Poetzel et al. 1992) near AFGL 2591. The distance of the source is not well established. Assuming a value of 1 kpc, it has a luminosity of $\sim 2 \cdot 10^4$ $L_\odot$ and an estimated stellar mass of 10 $M_\odot$.

5.5.2 Observations and data reduction

AFGL 2591 was observed with MIRAC3 at IRTF on June 3 and 4, 1999. We obtained images in the 11.6, 12.5 and 18.0 μm 10% passband filters, with a total on-source integration time of 600, 370 and 570 seconds respectively. The standard stars α Her and β Peg, observed before and after the science target, were used for flux and PSF calibration.

The data acquisition and reduction was performed as for the AGB sources of the previous sections. The background was removed by using a standard beam switching technique, with the source in all four beams. Each individual nod cycle required a 10 second on-source integration, and the procedure was repeated for as many cycles as needed to obtain the requested total integration time.

5.5.3 Results and discussion

A schematic drawing of AFGL 2591 and its related structures is given in figure 5.25.

The images of AFGL 2591 are shown in figure 5.26, 5.27 and 5.28. The central source is not clearly resolved. It has FWHM of 0.84", 0.87" and 1.21" at 11.7, 12.5 and 18.0 μm respectively. An extended knot of emission $\sim$6" SW from the central source is visible in all three images. A compact faint source is seen $\sim$11" NW of AFGL 2591. We list mid-IR fluxes for the

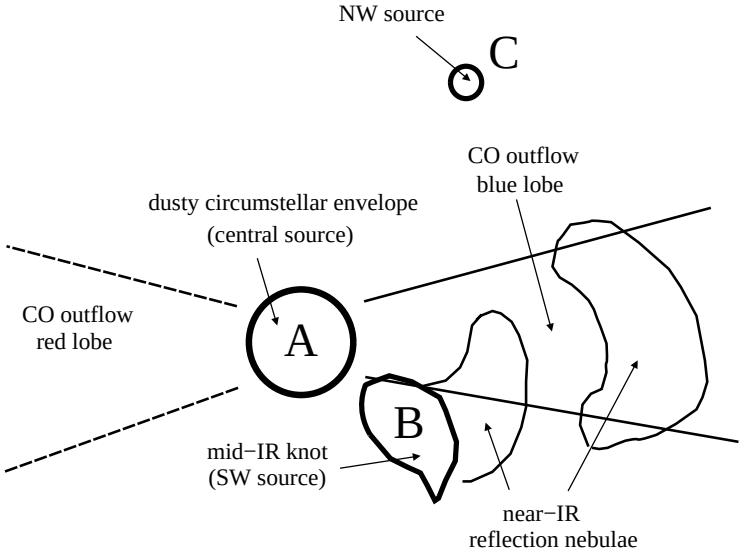

FIG. 5.25.— Schematic view of AFGL 2591 and related structures.

TABLE 5.8 PHOTOMETRY OF AFGL 2591

Source	$F_{11.7}$ [Jy]	$F_{12.5}$ [Jy]	$F_{18.0}$ [Jy]	T_{col} [K]
A	440	745	753	320
B	18.4	15.9	79.6	110
C	1.8	2.1	16.2	110

three sources in Table 5.8. From the 12.5 and 18.0 μm fluxes we derived color temperatures of 300–350 K for the central source, and 100–120 K for the SW knot and the NW source.

The only previously published observation of AFGL 2591 in the mid-IR was obtained with TIRCAM at SPM (Persi et al., 1995), and does not reveal the SW knot or the NW compact source seen in the MIRAC3 images.

The flux of the central source rises dramatically from 11.7 to 12.5 μm, implying that the 11.7 μm flux may be suppressed by a large silicate absorption feature at $\sim$9.8 μm. Indeed, the IRAS LRS of the source shows deep absorption at that wavelength. Thus, it is likely that the protostar is

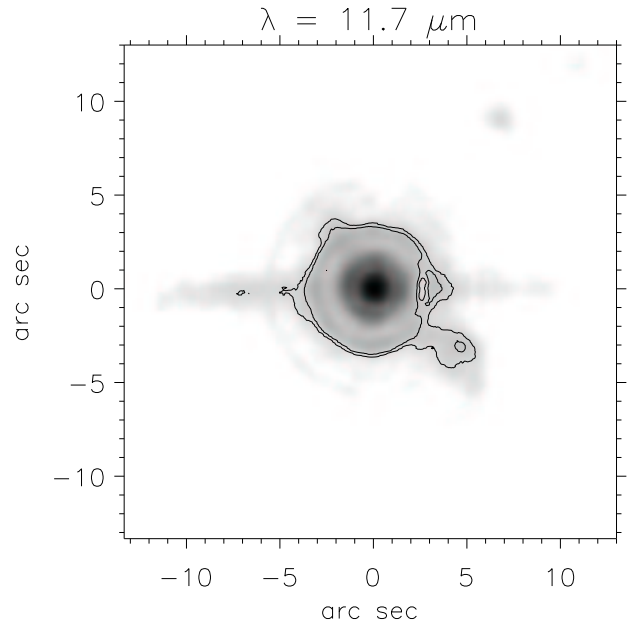

FIG. 5.26.— 11.7 μm image of AFGL 2591. Contours are plotted for 10 and 15 σ levels.

surrounded by an optically thick dusty envelope, perhaps in free fall collapse onto the star (van der Tak et al., 1999). Our observations limit the radius of the envelope to ∼2500 A.U.

Figure 5.29 shows the IRAS spectrum of the source, and the best fit we obtained by modeling the circumstellar envelope with DUSTY using the same technique described for the AGB envelopes of the previous chapters. The shown fit is for a spherically symmetric envelope with radial density profile $n(r) \propto r^{-2}$ around a central black body of $T_{eff} \simeq 25{,}000$ K (van der Tak et al., 1999). The fit with $n(r) \propto r^{-1.5}$ (i.e. constant infall) was not as good, implying that the infalling envelope is likely to be surrounded by a fair amount of non-infalling cloud material. The model spectrum is not particularly sensitive to the T_{eff} of the central source. Our best fit to the LRS suggests an A_B of the order of 100.

AFGL 2591 is generally considered an example of a relatively isolated massive star formation. However, our detection of a faint point source 11" NW of it suggests the presence of other embedded low mass stars in the vicinity. A preliminary look at the Two-Micron All Sky Survey (2MASS) J,H

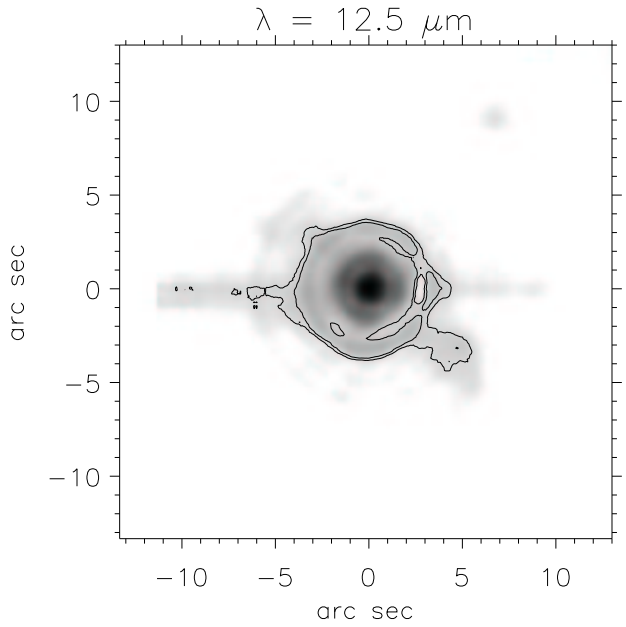

FIG. 5.27.— 12.5 μm image of AFGL 2591. Contours are plotted for 10 and 15 σ levels.

and K images reveals at least two other sources within 40" of AFGL 2591. Deep mid-IR images of a larger area are needed to search for a possible cluster of low-mass protostars in the region.

The SW knot we detect appears close to the inner portion of a loop first observed in the near-IR by Forrest & Shure (1986). The near-IR emission is assumed to arise from scattering of photons from the main source off dust grains at the surface of a cavity cleared by the outflow. The loop, also seen in NH_3 observations by Torrelles et al. (1989), is indeed located in the blue outflow lobe, i.e., the one toward us. At 18 μm we derive an optical depth $\tau_{18} \simeq 1.2$, and therefore a mass estimate of $\gtrsim 0.2$ $M_\odot$ for this knot.

The SW knot is also coincident with a radio source as well as a knot of H_2 emission. The radio source, detected using interferometers at the Very Large Array (Campbell, 1984) and the Owens Valley Radio Observatory (van der Tak et al., 1999), has approximately flat spectrum between 6.1 and 0.3 cm, and is interpreted as free-free emission from an optically thin HII region. The H_2 emission is seen in an image taken with the BEAR imaging spectrometer on the Canada-France-Hawaii telescope using a narrow band filter

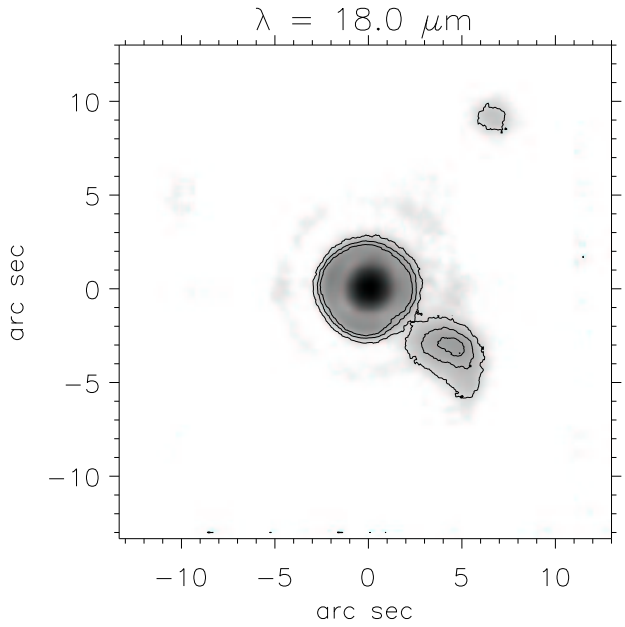

FIG. 5.28.— 18.0 μm image of AFGL 2591. Contours are plotted for 5, 10 and 15 σ levels.

on the 1-0 S(1) line, after the continuum is subtracted (G. Mitchell, personal communication). The existence of the H_2 line implies shock collisional heating of the molecular gas in the outflow, which provides the necessary excitation energy ($T \gtrsim 2000$ K, see e.g. Smith & Brand 1990). On the other hand, the dust responsible for mid-IR emission is characterized by a much lower temperature of $T_d \sim 100$ K, as inferred from our photometry. It is likely that the H_2 emission comes from the shock itself, while the mid-IR color temperature is determined by the local thermodynamical equilibrium of the dust with the radiation fiels (which has a much lower energy than the shock).

Previous near-IR observations have also revealed a second, larger loop of emission at a projected separation of ~ 19" from the star (Burns et al., 1989; Minchin et al., 1991; Tamura et al., 1991; Poetzel et al., 1992). The presence of multiple shells/loops is thought to be evidence for episodic mass loss outflows from AFGL 2591, as are molecular bullets seen in CO emission (Bachiller et al., 1991) and shocked knots observed in the optical and the near-IR (Reipurth, 1989) in other well known outflow sources. Up to $\sim 1 M_\odot$

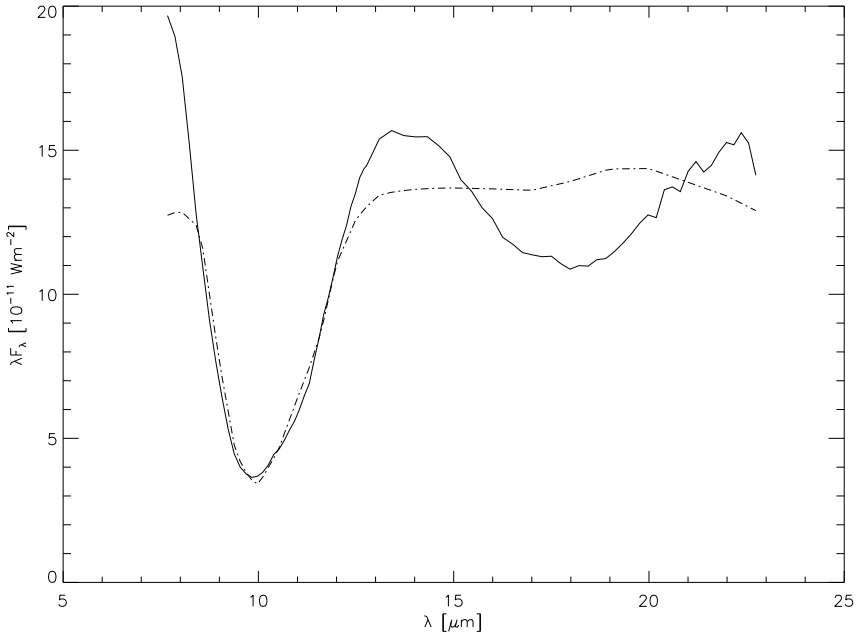

FIG. 5.29.— IRAS Low Resolution Spectrum of AFGL 2591 (thick line) and best fit model (dot-dashed line) for the 10 μm silicate feature. The heavy absorption is presumably due to an optically thick dusty envelope around the massive central star.

could be ejected in such eruptive events, though a few tenths of a solar mass is typical (Bachiller, 1996).

If we assume that the SW knot is associated with a recent mass ejection from AFGL 2591, we can estimate its dynamical timescale. Following Minchin et al. (1991), we take that the outflow is inclined from the plane of the sky by 55 degrees. In this case we estimate $\sim 10^4$ A.U. as the true distance from the star to the SW knot. Given a true outflow velocity of 26 km s^{-1} (based on the line of sight velocity of the CO gas observed by Bally & Lada 1983), we get a dynamical timescale of $\sim$ 2000 yr. For the same assumptions, the outer loop seen in the near-IR would have a dynamical timescale of $\sim$ 6000 yr. Such timescales are consistent with the estimated 10^4–10^5 yr total duration of the energetic outflow phase of YSOs (Bally & Lada, 1983).

In summary, our observations suggest that mid-IR imaging and spectroscopy can be powerful tools for probing the immediate circumstellar environment of embedded stars driving outflows. Such outflows appear to be

rather common around young stars and are very likely associated with accretion processes from the early stages of protostars. They may play an important role in determining the mass of the star-disk system, and affect the evolution of the surrounding molecular cloud. Yet our understanding of the outflow process is far from satisfactory. High-resolution imaging with current mid-IR cameras and future millimeter interferometers could help develop a more unified picture of infall and outflow in star formation.